Particuology 115 (2026) 174–191

Contents lists available at ScienceDirect

Particuology

journal homepage: www.elsevier.com/locate/partic

Sustainable glass-phase engineering via photovoltaic waste glass for enhanced energy storage in BNT ceramics

Truong Bach Chien, Le Phong Phu, Nguyen Chi Bao, Nguyen Ngoc Thien, Tran Thi Phuong Nghi, Thach Nguyen Phuc Khuong, Nguyen Hoc Thang*

Faculty of Chemical Engineering, Ho Chi Minh City University of Industry and Trade, 140 Le Trong Tan street, Tay Thanh ward, Ho Chi Minh City, 700000, Viet Nam

HIGHLIGHTS

- Photovoltaic waste glass enables sustainable BNT ceramic engineering.
- Dual role of glass phase controls conduction and microstructure.
- Grain boundary modification enhances dielectric breakdown strength.
- High energy density of 1.76 J/cm^3 achieved at 220 kV/cm.
- Improved efficiency via reduced remanent polarization.

GRAPHICAL ABSTRACT

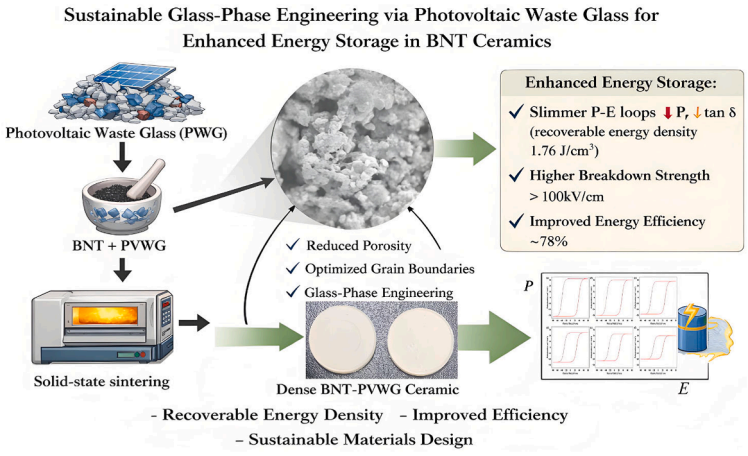

ARTICLE INFO

Keywords:
$Bi_{0.5}Na_{0.5}TiO_3$ (BNT)
Lead-free ferroelectric ceramic
Piezoelectric
Energy storage
Photovoltaic waste glass (PVWG)
Glass-phase engineering

ABSTRACT

Developing sustainable dielectric ceramics with high energy storage performance under a moderate electric field is still a great challenge for the next generation pulse power capacitors. Herein, recycled photovoltaic waste glass (PVWG) was added into $Bi_{0.5}Na_{0.5}TiO_3$ (BNT)-based lead-free ceramics via a conventional solid-state route and sintered at 1120 °C for 2 h. The PVWG additive facilitated liquid-phase sintering, reduced porosity, promoted grain-boundary homogeneity and improved the dielectric breakdown strength. Therefore, the optimized BNT-08 ceramic exhibits a high relative density of 97.04 ± 0.15 %, a reduced remanent polarization (P_r) of 9.4 ± 0.3 μC cm^{-2}, an increased breakdown strength (E_b ~220 ± 5 kV cm^{-1}) and a significantly slimmer P-E hysteresis loop. Hence, a recoverable energy density (W_{rec}) of 1.76 ± 0.07 J cm^{-3} and an energy storage efficiency of 78 ± 2 % were obtained under a moderate electric field at 220 kV cm^{-1}. The enhanced energy storage performance was ascribed to the synergistic effects of structural stabilization, defect-regulated charge transport, and PVWG-induced microstructural refinement. This simple, low cost and environmentally friendly method

* Corresponding author.
E-mail address: thangnh@huit.edu.vn (N.H. Thang).

https://doi.org/10.1016/j.partic.2026.05.014
Received 4 April 2026; Received in revised form 13 May 2026; Accepted 21 May 2026
Available online 26 May 2026

demonstrates PVWG as a promising multifunctional additive for electroceramic applications in line with the circular strategy.

1. Introduction

Electrostatic energy storage ceramics have gaining popularity for advanced pulsed power systems, electric vehicles, wearable electronics, and high-temperature capacitors because they can charge and discharge very quickly, have a high-power density, and are more stable at high temperatures than electrochemical energy storage technologies (Khan et al., 2025; Supriya, 2022). Ferroelectric and relaxor-based dielectrics are especially promising because their nonlinear polarization response lets them store a lot ofenergy (W_{rec}) even when there are strong electric fields (Zubairi et al., 2024). Nevertheless, high-performance ferroelectrics ceramics remain predominantly influenced by Pb-based systems, exemplified by $Pb(Zr,Ti)O_3$ (PZT), whose exceptional characteristics derive from morphotropic phase boundary engineering (Zhang, Han, et al., 2025). Concerns about lead effects of toxicity on health and the environment, along with stricter rules, have led to a lot of work on findings sustainable and lead-free alternatives (Njema et al., 2026; Ünsal et al., 2026). $Bi_{0.5}Na_{0.5}TiO_3$ (BNT) is widely regarded as one of the most promising lead-free ferroelectric materials owning to its significant spontaneous polarization, comparatively elevated Curie temperature (~320 °C), and pronounced ferroelectric distortion (Zhong et al., 2026). These inherent traits make BNT a good choice for storing dielectric energy. However, pure BNT has some built-in problems that make it less useful in real life (Kaarthik et al., 2026). When Bi and Na vaporize during high temperature processing, it causes non-stoichiometry and oxygen vacancy to form, which makes the leakage current go up (Ecebaş et al., 2026). Also, the moderate breakdown strength (E_b) limits the energy density that can be reached because W_{rec} increases the square of the applied electric field (Xie et al., 2026). And, the remanent polarization (P_r) is relatively high, which causes wide hysteresis loops. This lowers the efficiency (η) of energy storage and the ability to reverse polarization (Guan et al., 2024). Because of this, unmodified BNT usually does not store energy as well as the best relaxor ferroelectrics (Soheli et al., 2024). Consequently, formulating efficient strategies to concurrently mitigate leakage conduction, augment breakdown strength, and refine polarization behavior continues to be a significant challenge for BNT-based ceramics (Ecebaş et al., 2026; Guan et al., 2024; Soheli et al., 2024; Xie et al., 2026).

To mitigate these constraints, significant endeavors have been focused on the compositional and microstructural engineering of BNT ceramics. Researchers have looked into solid-solution modification, like making binary or ternary systems with $BaTiO_3$, $K_{0.5}Na_{0.5}NbO_3$, and other perovskites to make relaxor behavior and phase coexistence happen. This improves polarization dynamics and energy storage performance (Ravinshu et al., 2025; Zhang, Chen, et al., 2025). However, these kinds of methods often require complicated compositional design and could make thermal and structural stability worse (Zhang, Wei, et al., 2025). Rare-earth doping has also been used to control defect chemistry and local structural heterogeneity (Zheng et al., 2022). Dopants such as La^{3+}, Nd^{3+}, or Sm^{3+} have led to a lower concentration of oxygen vacancies and a better dielectric response (Azizi et al., 2025; Zheng et al., 2022). However, too much doping can make thecrystals less stable and add unwanted secondary phases, which can lower the dielectric breakdown strength (Chen et al., 2026). More advanced methods, like core-shell architechtures, have been suggested to conduction pathways and polarization switching, which greatly increases energy storage density (Yan et al., 2020; Zhang et al., 2026). However, these methods usually need complicated synthesis routes and exact control over the composition, which make them hard to scale up.

Glass-phase engineering has become a straightforward yet efficient method for modifying the microstructure and electrical characteristics of ferroelectric ceramics (Shi et al., 2023). Adding an amorphous intergranular phase can help liquid-phase sintering, make things denser, and improve the microstructure (Tang et al., 2023). More importantly, insulating glassy phases at grain boundaries can stop the flow of charge carriers, even out the local electric field, and slow down dielectric breakdown (Shi et al., 2023; Tang et al., 2023). This makes energy storage more efficient (Yang et al., 2022). Even though these are good things, most of the studies that came before this one used glass systems that were made for commercial use (like borosilicate or alkali silicate glasses) and focused more on improving densification than on basic structure-property relationships. Recent study of Ouaha et al. (2024) showed that adding Nb-Bi-Ti-P-based glass to BNT ceramics can improve their dielectric properties and energy storage performance by changing the way the grains interact with each other (Ahmed et al., 2024). Nonetheless, these studies continue to depend on engineered glass compositions and fail to explore the potential of waste-derived multi--component glass systems. More importantly, how complex glass chemistry affects defect states, grain boundary potential barriers, and breakdown mechanisms which still do not know enough. Also, the sustainability part of glass-phase engineering has mostly been ignored.

As the photovoltaic industry grows quickly, the problem of too many old solar panels is becoming a major environmental issue (Nguyen et al., 2024). Photovoltaic waste glass (PVWG), which makes up a large part of the waste from solar panels, is mostly made up of SiO_2, but it also has a lot of CaO, Al_2O_3, Na_2O, and small amounts of functional oxides that were added during the glass-making process (Nguyen et al., 2024). PVWG is a complex multi-component system that can change defect chemistry, grain boundary characteristics, and interfacial electrical behavior. This is different from regular commercial glass additives. Although the waste glass recycling has been investigated in construction materials and traditional ceramics, its use as a functional additive in advanced ferroelectric energy storage materials is still largely unexamined (Chakrabarti et al., 2022; Nguyen et al., 2024). There is currently no comprehensive study examining the use of photovoltaic waste glass as a glass-phase engineering agent to concurrently regulate microstructure, defect chemistry, and energy storage performance in BNT ceramics. Current research primarily concentrates on either enhancing densification or optimizing electrical performance, failing to develop a holistic structure-property-performance relationships (Ahmed Althumairi et al., 2025; Gao et al., 2025; Li et al., 2024). Additionally, the relationship between mechanical robustness and dielectric reliability, which is critical for practical capacitor applications, has not been adequately explored in BNT-based systems (Wu et al., 2025; Zhou et al., 2023). These gaps show that the studies need a long-term and mechanistically informed plan that combines waste valorization with functional material design (Rehman et al., 2025; Weinmann et al., 2025).

In this context, the present study suggests a sustainable glass-phase engineering methodology by integrating photovoltaic waste glass (2-10 wt%) into BNT ceramics. PVWG is expected to do two things that regular glass additives do not: (i) speed up liquid-phase sintering and microstructural densification, and (ii) change the chemistry of grain boundary and distribution of defects because it is made up of more than one component. This study seeks to clarify the correlation among amorphous phase fraction, grain boundary structure, defect-mediated conduction, and dielectric breakdown behavior through systematic variation of the PVWG content. A specific focus is placed on comprehending the impact of the amorphous intergranular phase on leakage suppression, electric field homogenization, polarization reversibility, and ultimately the recoverable energy density. By combining structural, microstructural, mechanical, and electrical analyses, this study shows a possible way to make good use of photovoltaic waste and also gives new

information about how glass-phase-regulated energy storage works in lead-free ferroelectric ceramics. The results are anticipated to aid in the advancement of high-efficiency, sustainable dielectric materials for next-generation electronic and pulsed power applications.

2. Materials and methods

2.1. Raw materials and photovoltaic waste glass processing

This study used high-purity Bi_2O_3 (≥99.9%), TiO_2 (anatase phase, ≥99%), and NaOH (≥98%) from Sigma-Aldrich as starting materials for synthesizing $Bi_{0.5}Na_{0.5}TiO_3$ (BNT). NaOH was chosen instead of Na_2CO_3 as sodium source in traditional solid-state routes to improve reaction homogeneity and make solid-state diffusion easier. Using NaOH also stops CO_2 from coming out during calcination, which lowers carbonate-related porosity and makes phase purer (Ecebaş et al., 2026). After the metal frames and polymeric encapsulants were taken off, photovoltaic waste glass (PVWG) was collected from end-of-life solar panels. The recovered glass was cleaned with ultrasound in deionized water, dried at 100 °C, and then ground into fine powder with particle size smaller than 45 μm. The chemical composition of PVWG, determined by X-ray fluorescence (XRF) using S2 PUMA (Brucker, German) to find out what chemicals were in PVWG. Table 1 shows that PVWG is mostly made up of SiO_2 (about 70.1 wt%), with large amounts of Na_2O (~11.3 wt%) and CaO (~11.4 wt%), and small amounts of Al_2O_3, MgO and Fe_2O_3 as reported in (Nguyen et al., 2024). Because it has more than one type of silicate, PVWG can be both a low-melting glass-phase former and intergranular insulating additive.

It is important to note that PVWG is expected to have two functions, unlike regular single-purpose glass additives. First, it will help with liquid-phase sintering because it has a relatively low softening temperature (about 700-800 °C). Second, it will change the chemistry of grain boundaries and the distribution of defects because it is made up of multiple oxides. The dual functionality is the main focus of this study, where PVWG is used as a controllable amorphous phase engineering agent instead of just a way to make things denser.

2.2. Sample preparation

BNT-based ceramics were prepared with different amounts of PVWG using a standard solid-state reaction method. Stoichiometric amounts of Bi_2O_3, NaOH, and TiO_2 were mixed with PVWG powders (0-10 wt%), and then ball-milled in ethanol for 12 h using zirconia milling media to make sure the mixing was even. The compositions were labeled BNT-00, BNT-02, BNT-04, BNT-06, BNT-08, and BNT-10, which stand for 0, 2, 4, 6, 8, and 10 wt% PVWG addition, respectively as shown in Table 2.

After drying the powders were pressed into cylindrical pellets with a diameter of about 18 mm and a thickness of around 2 mm. This was done with a pressure of 10 MPa. The green compacts were first heated in air at temperature of 800 °C for 4 h to help the perovskite BNT phase form as shown in Fig. 1. After that, the calcined powders were ground lightly, pressed again, and sintered at 1120 °C for 2 h, with a heating rate of 5 °C/min and natural cooling to room temperature. It is worth to mention that PVWG, although it can soften at temperatures around 700-800 °C, is present in low concentrations (≤10 wt%) and solid-state reaction kinetics dominate, so that the formation of the perovskite phase is not impeded during calcination. PVWG plays a role in liquid phase assisted densification primarily in the later stage of sintering process. Finally, the samples of BNT and PVWG-doped BNT ceramics were tested for engineering properties such as electrical and mechanical properties, and characterized for microstructure.

Table 1
Chemical composition of photovoltaic waste glass (PVWG).

Oxides	SiO_2	Na_2O	CaO	Al_2O_3	MgO	Fe_2O_3	Others	L.O.I
wt %	70.1	11.3	11.4	1.6	3.2	1.9	0.2	0.3

2.3. Structural and microstructural characterization

The phase composition and crystal structure of the synthesized BNT-PVWG ceramics were studied using X-ray diffraction (XRD) (D2 Phaser, Brucker AXS, Germany) with Cu Kα radiation ($\lambda = 1.5406$ Å) operating at 30 kV and 10 mA. Diffraction patterns in the 2θ range of 5°-80° with a scanning step of 0.02° were recorded. The crystalline index (CI) from the X-ray diffraction (XRD) patterns was employed to calculate the crystallinity of the BNT-PVWG ceramics. The CI was calculated as the ratio of the integrated intensity of crystalline peaks to the total diffracted intensity, including contributions from both crystalline and amorphous phases. The crystallinity index was calculated by using the following equation (Gilmore et al., 2019):

$$CI = \frac{A_c}{A_c + A_a} \times 100\%$$

where A_c represents the integrated area of crystalline diffraction peaks and A_a corresponds to the integrated area of amorphous background.

The XRD patterns were imported into Origin software (OriginPro, OriginLab Corp.) for quantitative analysis. Baseline correction was applied to eliminate background noise and overlapping diffraction peaks were deconvoluted by peak fitting with Gaussian or pseudo-Voigt functions. The crystalline peak areas (A_c) were determined from the integral of all fitted Bragg reflections corresponding to the perovskite phase. The amorphous contribution (A_a) was determined from the broad diffuse scattering hump with observation in the 2θ range of ~5°-80°, which is assigned to the glassy PVWG phase. The baseline was removed and the area under the XRD curve was computed and the CI value was calculated from the ratio of crystalline area to the total area. To ensure reproducibility, the fitting procedure was consistently performed on all samples with identical fitting parameters and peak selection criteria. The calculated CI gives a semi-quantitative measure of relative crystallinity and allows to assess the effect of PVWG addition on the evolution of amorphous and crystalline phases in the BNT matrix.

Prior to crystallite size and lattice strain calculations, instrumental broadening was determined using a standard silicon reference and subtracted from the measured peak widths. The crystallite size was calculated by Scherrer equation and the lattice strain was determined from the peak broadening analysis. The values given are mean values from several diffraction peaks and errors were taken into account to ensure the reliability. It is reported BNT has a rhombohedral or pseudo-cubic structure at room temperature. For simplicity, the diffraction patterns in this study were analyzed in terms of an average pseudo-cubic perovskite symmetry, although local structural distortions are possible.

2.3.1. Crystallite size

The average crystallite size, D was estimated using the Scherrer equation (Cao Hien et al., 2025; Khoi & Thang, 2026):

$$D = \frac{K\lambda}{\beta\cos\theta}$$

where K is the Scherrer constant (K = 0.9); λ is the X-ray wavelength ($\lambda = 1.5406$ Å); β is the full width at half maximum (FWHM) of the diffraction peak (in radians); and θ is the Bragg diffraction angle.

2.3.2. Lattice strain

The microstrain (ε) present in the crystal lattice was estimated from peak broadening using (Cao Hien et al., 2025):

$$\varepsilon = \frac{\beta}{4\tan\theta}$$

This parameter reflects local lattice distortions caused by defects or compositional heterogeneity.

Table 2
Composition and processing conditions of PVWG-doped BNT ceramics.

No.	Samples	NaOH (%)	Bi_2O_3 (%)	TiO_2 (%)	PVWG (%)	Calcination conditions	Sintering condition
01	BNT-00	9.24	53.84	36.92	0.00	800 °C, 4 h	1120 °C, 2 h
02	BNT-02	9.06	52.76	36.18	2.00	800 °C, 4 h	1120 °C, 2 h
03	BNT-04	8.87	51.69	35.44	4.00	800 °C, 4 h	1120 °C, 2 h
04	BNT-06	8.69	50.61	34.70	6.00	800 °C, 4 h	1120 °C, 2 h
05	BNT-08	8.50	49.53	33.97	8.00	800 °C, 4 h	1120 °C, 2 h
06	BNT-10	8.32	48.45	33.23	10.00	800 °C, 4 h	1120 °C, 2 h

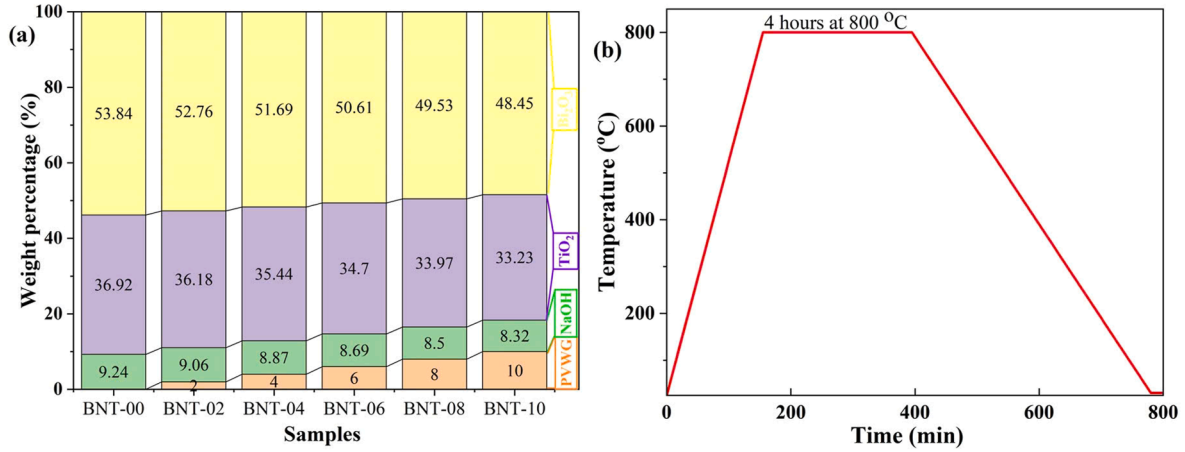

Fig. 1. Changes in the composition of photovoltaic waste glass (PVWG) in the mixing ratios of the samples (a) and the first stage of calcination curve for BNT and PVWG-doped BNT samples (b).

2.3.3. Dislocation density

The dislocation density (δ), representing the amounts of crystallographic defects in the lattice, was calculated from the crystallite size using (Cao Hien et al., 2025; Gilmore et al., 2019):

$$\delta = \frac{1}{D^2}$$

where D is the crystallite size obtained from the Scherrer equation.

2.3.4. Crystal plane indexing

For cubic systems, the interplanar spacing d_{hkl} is related to the lattice parameter a and the Miller indices (hkl) by (Gilmore et al., 2019):

$$d_{hkl} = \frac{a}{\sqrt{h^2 + k^2 + l^2}}$$

The lattice parameter a can therefore be calculated from the measured d_{hkl} values as (Gilmore et al., 2019):

$$a = d_{hkl}\sqrt{h^2 + k^2 + l^2}$$

The interplanar spacing, d_{hkl} was determined using Bragg's law (Gilmore et al., 2019):

$$n\lambda = 2d\sin\theta$$

where n is the diffraction order (typically $n = 1$), λ is the X-ray wavelength ($\lambda = 1.5406$ Å), and θ is the Bragg diffraction angle.

2.3.5. Atomic packing factor (APF)

For an ideal cubic perovskite structure, the atomic packing factor (APF) describes the fraction of the unit cell volume occupied by atoms and can be estimated as (Gilmore et al., 2019):

$$APF = \frac{\sum V_{atoms}}{V_{cell}}$$

For the cubic perovskite structure ABO_3, the unit cell volume is, $V_{cell} = a^3$, with a is the lattice constant.

2.3.6. Bond length calculations

For the cubic perovskite structure ABO_3 ($Pm\bar{3}m$), the bond lengths between the A-site cation and oxygen ($L_{A–O}$) and between the B-site cation and oxygen ($L_{B–O}$) can be calculated geometrically from the lattice parameter.

The B–O bond length is $L_{B-O} = \frac{a}{2}$ and the A–O bond length is $L_{A-O} = \frac{a}{\sqrt{2}}$

These parameters provide insight into octahedral distortion and structural stability within the perovskite lattice.

2.3.7. Goldschmidt tolerance factor

The structural stability of the perovskite lattice was evaluated using the Goldschmidt tolerance factor (Gilmore et al., 2019):

$$t = \frac{r_A + r_O}{\sqrt{2}(r_A + r_O)}$$

where r_A is the ionic radius of the A-site cation; r_B is the ionic radius of the B-site cation; r_O is the ionic radius of oxygen. For an ideal cubic perovskite structure, the tolerance factor typically lies within the range of $0.9 < t < 1.0$. These values close to unity indicate a stable cubic structure.

2.3.8. Theoretical density

The theoretical density (ρ_{th}) of the perovskite unit cell was calculated using (Gilmore et al., 2019):

$$\rho_{th} = \frac{Z \times M}{N_A \times a^3}$$

where Z is the number of formula units per unit cell ($Z = 1$ for cubic perovskite ABO_3); M is the molar mass of the formula unit; N_A is Avogadro's number; and a is the lattice constant.

The calculated structural parameters provide important insight into

the structural evolution of BNT ceramics with PVWG incorporation. In particular, variations in lattice constant, crystallite size, and lattice strain reflect subtle modifications in the perovskite framework. Additionally, the tolerance factor and bond length calculations help to evaluate the structural stability of the BNT lattice and the influence of compositional modification on octahedral geometry. These structural features are closely related to the observed electrical conduction behavior and energy storage performance discussed in subsequent sections.

The bonding configuration and local structural vibrations in the BNT-PVWG ceramics were further analyzed by Fourier transform infrared spectroscopy (FTIR) (FT/lR-6X FTIR spectrometer, JASCO, Japan). FTIR spectra were recorded in the wavenumber range of 400-4000 cm^{-1} at a resolution of 4 cm^{-1} with 32 scans per sample. The powdered ceramic samples were mixed with KBr and pressed into pellets. The characteristic vibrational bands related to Ti-O and Ti-O-Ti bonds were analyzed to confirm the perovskite structure and Si-O bands were used to evaluate the incorporation of the glass phase.

The microstructural characteristics of the sintered ceramics were analysized using scanning electron microscopy (SEM) (JEOL JSM-IT200, Japan) at an accelerating voltage of 10 kV. The ceramic samples were mechanically polished and coated by a super-thin gold layer corresponding to good observation and obtain high quality images. Grain size distribution was quantified by measuring more than 200 grains using image analysis software (ImageJ), and the results are reported as mean grain size ± standard deviation.

2.4. Physical and mechanical property measurements

The physical properties of the sintered BNT-PVWG ceramics were evaluated through bulk density and apparent porosity measurements using the Archimedes method. Prior to measurement, the ceramic samples were cut into rectangular specimens and their surfaces were carefully polished to remove irregularities. The bulk density (ρ_{bulk}) was determined by measuring the dry mass, suspended mass in distilled water, and saturated mass of the samples. The apparent porosity and water absorption were subsequently calculated according to standard Archimedes equations. The relative density of the ceramics was obtained by comparing the measured bulk density with the theoretical density of the BNT-based perovskite structure. Statistical reliability was ensured by testing each composition with a minimum of three specimens ($n \geq 3$). The Vickers hardness of the ceramics was measured using a microhardness tester (HMV-G21, Shimadzu, Japan) with a constant load of 1 kgf and a dwell time of 15 s. The Vickers hardness (H_v) was calculated from the diagonal lengths of the indentation marks using the standard relation between applied load and indentation area. At least five indents were made for each sample and the average value with standard deviation was reported.

Fracture toughness (K_{IC}) was calculated using the indentation fracture method based on the Anstis model:

$$K_{IC} = 0.016\left(\frac{E}{H}\right)^{1/2}\frac{P}{c^{3/2}}$$

where P is the applied load, c is the crack length, E is Young's modulus and H is the hardness. This method allows us to reliably evaluate the crack resistance of brittle ceramics.

This method provides a convenient approach to evaluate the resistance of the ceramics to crack propagation. The combined analysis of density, porosity, hardness, and fracture toughness allowed for the evaluation of the densification behavior and mechanical integrity of the BNT-PVWG ceramics. In particular, the influence of PVWG addition on liquid-phase-assisted sintering and microstructural consolidation was assessed by correlating the physical and mechanical parameters with the microstructural observations obtained from SEM analysis.

2.5. Electrical characterization and conduction analysis

The electrical properties of the PVWG-doped BNT ceramics were investigated using temperature-dependent conductivity measurements. Electrical contacts were formed by coating both sides of the sintered pellets with silver paste (SPI Supplies), followed by firing at 500 °C for 30 min. The electrical conductivity was measured using an LCR meter (Agilent E4980A) in a temperature range 300-600 K at a frequency of 1 kHz with an AC voltage amplitude of 1 V. The temperature was controlled using a programmable furnace with a heating rate of 2 °C/min to ensure enough time for stabilization at each temperature. The temperature dependence of conductivity was analyzed by Arrhenius relation (Petrowsky & Frech, 2009):

$$\sigma = \sigma_0 \exp\left(-\frac{E_a}{kT}\right)$$

where σ is the electrical conductivity, σ_0 is the pre-exponential factor, E_a is the activation energy for electrical conduction, k is the Boltzmann constant ($k = 8.617 \times 10^{-5}$ eV/K), and T is the absolute temperature. By plotting lnσ as a function of the reciprocal temperature ($1000/T$), the activation energy associated with charge transport processes was determined from the slope of the linear Arrhenius plots.

This analysis provides insight into the dominant conduction mechanisms in the BNT-PVWG ceramics. In particular, the influence of PVWG addition on grain boundary characteristics, defect concentration, and charge carrier mobility was evaluated. The resulting activation energies were compared among different compositions to understand how the incorporation of the glass phase modifies electrical transport pathways within the ceramic matrix.

2.6. Energy storage and ferroelectric measurements

The energy storage properties of the PVWG-doped BNT ceramics were evaluated through polarization-electric field (P-E) hysteresis loop measurements at room temperature by a ferroelectric analyzer (Precision Premier II, Radiant Technologies, USA). A triangular wave with a frequency of 10 Hz was applied to record ferroelectric hysteresis (P-E) loops. The sample thickness was carefully measured so that the applied electric field could be accurately calculated. The applied electric field was increased stepwise to a maximum value of 220 kV/cm. Each composition was tested in at least five samples ($n \geq 5$) for reproducibility. Prior to measurement, the ceramic pellets were polished and coated with silver electrodes on both surfaces to ensure uniform electric field distribution across the sample. The polarization behavior was analyzed in terms of key ferroelectric parameters, including maximum polarization (P_{max}), remanent polarization (P_r), and coercive field (E_c). The integrated area of the P-E loops was used to calculate energy storage density (W_{rec}) and efficiency (η).

The energy storage performance of the ceramics was calculated directly from the measured P-E loops. The calculated recoverable energy density (W_{rec}) corresponds to the area enclosed between the discharge curve and the polarization axis and can be expressed as (Li et al., 2020):

$$W_{rec} = \int_{P_r}^{P_{max}} EdP$$

while the total stored energy density (W_{total}) is determined from the integral of the entire charging curve. The energy storage efficiency (η) was subsequently calculated using (Li et al., 2020):

$$\eta = \frac{W_{rec}}{W_{total}} \times 100\%$$

These parameters provide a quantitative measure of the capability of the material to store and release electrical energy. In addition, the dielectric breakdown strength (E_b) of the ceramics was defined as the maximum electric field that the sample could withstand before electrical

breakdown. Measurements were performed in silicone oil to avoid surface flashover and to enable the intrinsic dielectric breakdown. The influence of PVWG incorporation on the energy storage behavior was analyzed by correlating the ferroelectric parameters with the structural, microstructural, and electrical characteristics of the ceramics. In particular, the reduction in remanent polarization, improvement in breakdown strength, and modification of grain boundary characteristics were examined as key factors contributing to the enhanced recoverable energy density and energy storage efficiency observed in the optimized compositions.

3. Results and discussion

3.1. Structural evolution and crystal-lattice modulation of PVWG-doped BNT ceramics

The crystallographic evolution of $Bi_{0.5}Na_{0.5}TiO_3$ (BNT) ceramics with increasing content of photovoltaic waste glass (PVWG) was systematically studied by X-ray diffraction (XRD) as shown in Fig. 2. All compositions display well-defined diffraction peaks that are characteristic of a perovskite-type structure and no secondary crystalline phases related to bismuth oxides, sodium titanate, or silicate crystalline phases are detected within the resolution limit of the instrument. This observation confirms that the introduced PVWG does not crystallize into separate phases, but is predominantly retained as an amorphous intergranular component, in line with the behavior of silicate-based glass additives in oxide ceramics. The diffraction patterns can be indexed by a cubic perovskite model ($Pm\bar{3}m$), but a more rigorous interpretation is required. It is known that BNT at room temperature is usually rhombohedral (R3c) or mixed rhombohedral-tetragonal. In the present case, the lack of apparent peak splitting around the characteristic reflections (200) or (211/213), combined with the obvious peak broadening, indicates the long-range symmetry distortion is suppressed or averaged out. As such, the structure is more appropriately described as pseudo-cubic, which is a commonly used description for BNT-based systems exhibiting structural disorder or compositional heterogeneity (Rehman et al., 2025; Wu et al., 2025; Zhou et al., 2023). This clarification removes the ambiguity of the assignment of a purely cubic phase and is in agreement with established crystallographic understanding. The characteristic reflections observed at approximately $2\theta \approx 22.8°$, 32.4°, 40.1°, 46.6°, and 57.9° correspond to the typical (100), (110), (111), (200), and (210) crystallographic planes of the perovskite BNT lattice.

For the quantitative description of the structure evolution detailed analysis of the most intense (110) reflection was performed (Fig. 3(a)). The broadening and the position of maximum are gradually varied with increasing PVWG content which implies the simultaneous variation in the crystallite size and lattice strain. The instrumentalbroadening was calculated with a standard silicon reference and subtracted from the measured full width at half maximum (FWHM) for reliability of these calculations. The corrected FWHM values were then plugged into the Scherrer equation and strain calculations. The inclusion of instrumental correction and error estimation greatly enhances the robustness and reproducibility of the structural parameters obtained.

Quantitative phase analysis based on the integrated intensity ratio was performed to determine the relative proportion of crystalline and amorphous phases in the BNT-PVWG ceramics. Crystalline peaks were separated from the amorphous halo by fitting the diffraction profiles to pseudo-Voigt functions in Origin software after baseline subtraction. The results summarized in Fig. 3(b) demonstrate that the crystalline fraction decreases progressively as the PVWG content increases. The crystalline index shows a gradual decrease in crystallinity from 98.48% for BNT-00 to 95.28%, 94.81%, 92.36%, 90.63%, and 87.57% for BNT-02, BNT-04, BNT-06, BNT-08, and BNT-10, respectively corresponding to increase in amorphous content from 1.52% to 12.43% (Fig. 3(b)). This method is a semi-quantitative evaluation and not a full Rietveld refinement. However, the same fitting parameters were used for all compositions to get reliable comparative information. These results confirm the progressive formation of an intergranular glassy phase as increasing amounts of PVWG are added. The formation of such an intergranular amorphous network is expected to influence both microstructural evolution and electrical behavior by modifying grain boundary chemistry and charge transport pathways.

The calculated crystallite size increases from 19.36 nm for the undoped BNT sample to 22.16 nm, 24.46 nm, 26.17 nm, 27.86 nm, and

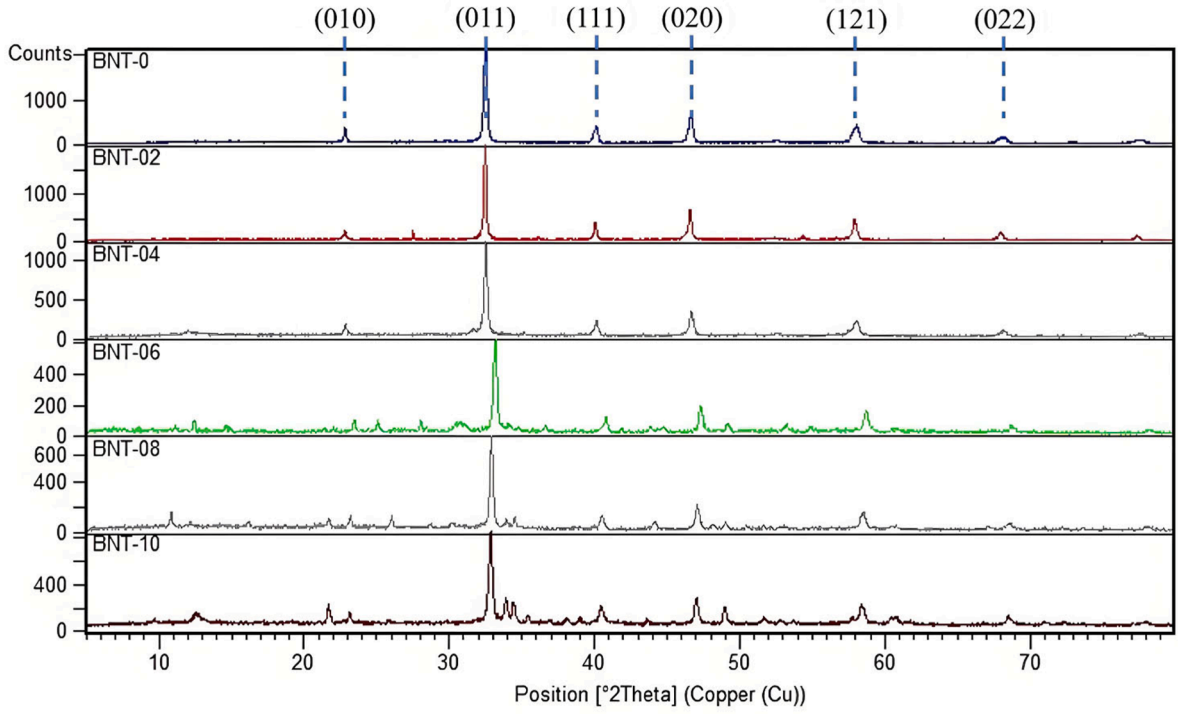

Fig. 2. XRD patterns of BNT samples with increasing PVWG content confirmed formation of pseudo-cubic perovskite crystal system with space group $Pm\bar{3}m$.

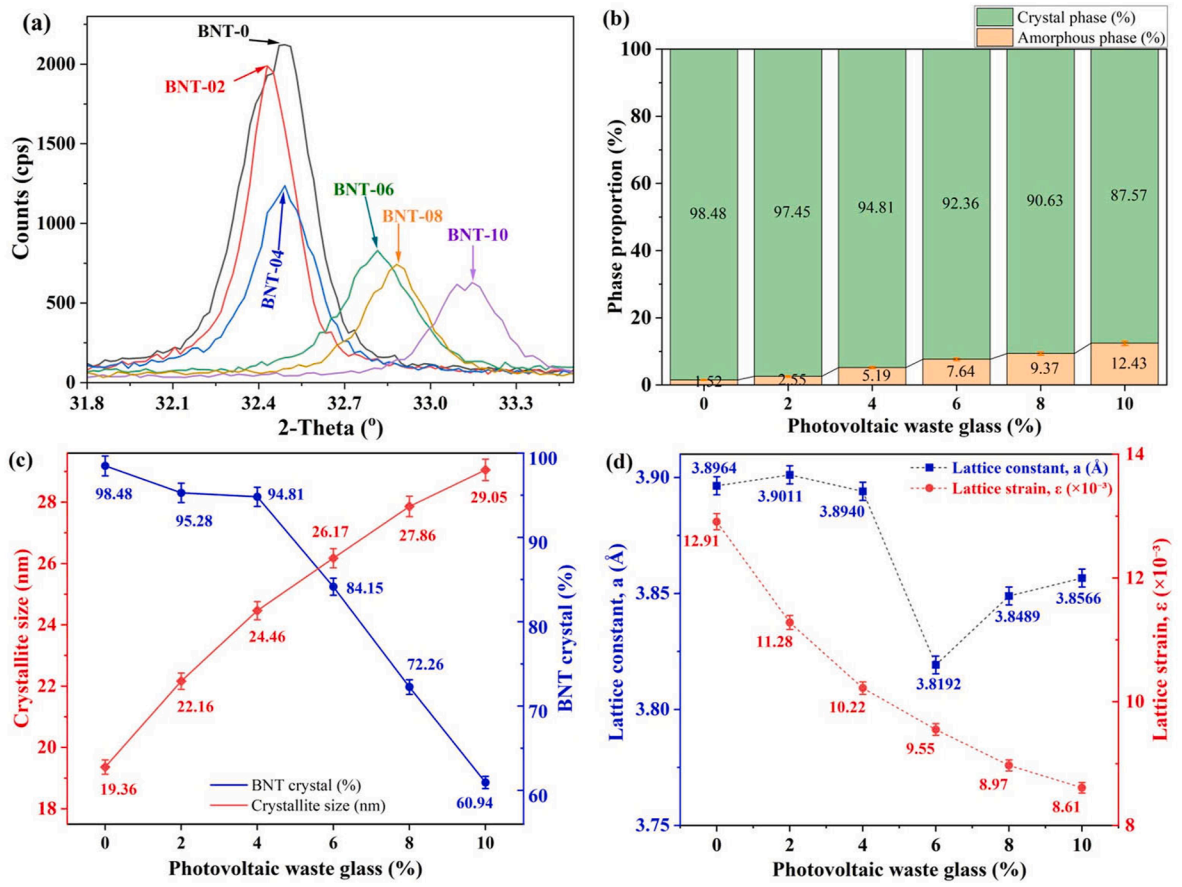

Fig. 3. XRD-derived structural parameters of BNT-PVWG ceramics with effects of PVWG to highest diffraction peak evolution of (011) plane (a); crystalline/amorphous phase fraction (b); crystallite size and BNT crystal content (c); and lattice constant and lattice strain (d).

29.05 nm for PVWG contents of 2%, 4%, 6%, 8%, and 10%, respectively (Fig. 3(c)). Importantly, error bars from multiple peak fittings have been added and show that apparent monotonic increase has measurable experimental scatter and is not an ideal linear trend. The increase in crystallite size is ascribed to the liquid phase assisted sintering induced by PVWG. The relatively low softening temperature of silicate glass and the partial softening of the PVWG phase during sintering is conducive to atomic diffusion and the coarsening of crystallites.

In addition to crystallite growth, the crystal content of the BNT phase also exhibits a gradual decrease with increasing PVWG concentration, declining from 98.48% to 60.94% as shown in Fig. 3(c). This reduction reflects the progressive dilution of the crystalline network by the amorphous glass phase. Nevertheless, the persistence of strong diffraction peaks across all compositions indicates that the perovskite framework remains the dominant structural component even at the highest PVWG loading. The evolution of the lattice constant and lattice strain extracted from the XRD refinement is presented in Fig. 3(d). The changes in lattice parameter and microstrain make the structural response of the BNT lattice even clearer. The undoped BNT sample displays a lattice constant of 3.8964 Å, which slightly increases to 3.9011 Å for BNT-02, indicating a minor lattice expansion at low PVWG concentration. However, as the PVWG content increases further, the lattice parameter gradually decreases to 3.8940 Å (BNT-04) and 3.8192 Å (BNT-06), followed by a slight recovery to 3.8489 Å (BNT-08) and 3.8566 Å (BNT-10). The initial lattice expansion may arise from local structural relaxation induced by the presence of glass-derived ions or interfacial stress between the amorphous phase and the crystalline BNT grains. In contrast, the subsequent lattice contraction observed at higher PVWG concentrations suggests increased lattice distortion and strain relaxation within the perovskite framework.

There are several competing reasons why the lattice constant variation does not follow a monotonic trend as PVWG content increases. Lattice distortion and contraction may be caused at low PVWG levels by the addition of aliovalent ions (like Si^{+} or Al^{3+}) and the creation of oxygen vacancies. However, peak shifting and broadening in XRD patterns can result in apparent lattice expansion at higher PVWG concentrations due to the existence of an amorphous glass phase and internal residual stresses. Peak position determination may also be uncertain due to the overlap between crystalline peaks and the amorphous background. Therefore, the lattice constant changes in a way that is not always predictable. This is because of the complicated interactions between defect chemistry, interfacial stress, and partial amorphization.

More importantly, the lattice strain drops significantly from 12.91×10^{-3} in BNT-00 to 11.28×10^{-3}, 10.22×10^{-3}, 9.55×10^{-3}, 8.97×10^{-3}, and 8.61×10^{-3} for increasing PVWG content (Fig. 3d). This shows that stress is effectively relaxing in the crystalline lattice. The glassy phase located at grain boundaries acts as a compliant interfacial layer that accommodates structural mismatch between neighboring grains, thereby reducing local distortion and defect concentration. This trend seems to be at odds with the FTIR results at first glance. The FTIR results show that the peaks are getting wider (Section 3.2), which means that there is more local structural disorder around the TiO_6 octahedra. However, it can be explained this apparent difference by looking at the different length scales that the two methods look at. XRD shows the average strain of the lattice over a long distance, while FTIR shows how sensitive it is to short-range local bonding environments. Incorporating PVWG, therefore, decreases global lattice distortion while simultaneously introducing local structural heterogeneity, especially at grain boundaries and amorphous-crystalline interfaces. This study also used the Williamson–Hall method to figure out the size of the crystallites and

the strain in the lattice, as shown in Table 3. The goal of this is to make sure that the values found using the Scherrer method are correct.

To further separate the effects of crystallite size and lattice strain on peak broadening, Williamson-Hall (W-H) analysis was done on several diffraction peaks, such as (010), (011), (111), (020), (121), and (022). To fix the instrumental broadening, a standard silicon reference was used first. Then, the corrected FWHM values were used to fit the data linearly using the Williamson-Hall equation. The calculation data were linear for all compositions, which means that the peak broadening is caused by a combination of the size of the crystallites and the strain in the lattice. The W-H results show that the crystallite size goes from about 18.7 nm to 28.8 nm as the PVWG content goes up. This is in line with what the Scherrer equation says, but the change is a little smaller because the strain effects are separated. The lattice strain, on the other hand, goes down from 13.2×10^{-3} to 8.5×10^{-3}, which shows that the lattice is relaxing more and more. The agreement between Scherrer and W-H trends confirms the accuracy of the structural analysis, while the W-H method gives a more physically meaningful description by taking into account broadening caused by strain. This study shows that adding PVWG helps crystallites grow while also reducing lattice distortion. This is probably because the liquid phase helps with sintering and stress relaxation at grain boundaries.

It is also important to know the difference between the size of the crystallites measured by XRD and the size of the grains seen in SEM analysis. The first one shows coherent diffraction domains, usually at the nanometer scale. The second one shows microstructural features at the micrometer scale. Even though both parameters changed when PVWG is added, their physical meanings are very different, and their relationship should be looked at in a qualitative way rather than a quantitative way.

The structural parameters derived from the XRD data are summarized in Table 4, which includes the dislocation density (δ), atomic packing factor (APF), bond lengths ($L_{A–O}$ and $L_{B–O}$), tolerance factor (t), and theoretical density (ρ_{th}). The decrease in dislocation density from 2.668×10^{-3} nm^{-2} for BNT-00 to 1.185×10^{-3} nm^{-2} for BNT-10 that comes with the decrease in lattice strain shows that the crystallinity has improved and the number of defects has gone down.The calculated bond lengths (A-O and B-O) show small differences, which means that the TiO_6 octahedral framework may have been slightly changed. The A-O bond length varies from 2.755 Å in BNT-00 to approximately 2.727 Å in BNT-10, while the B-O bond length decreases from 1.948 Å to 1.928 Å. Also, the tolerance factor (t), which is based on Shanon ionic radii (coordination number CN = 12 for A-site and CN = 6 for B-site) and the average of Bi^{3+} and Na^{+}, stay between 0.968 and 0.985. These values confirm that the perovskite framework is stable, but they do not mean that is has a strictly cubic symmetry. This supports the idea that it is pseudo-cubic. Similar tolerance factor values have been reported in previous studies on BNT-based ferroelectric ceramics (Li et al., 2020; Rehman et al., 2025; Wu et al., 2025; Zhou et al., 2023), where structural stability is maintained even in the presence of various dopants or compositional modifications.

Another important parameter obtained from the structural analysis is the atomic packing factor (APF), which remains within the range 0.739-0.748 for all samples. These values are typical for pseudo-cubic perovskite structures and indicate that the packing density of the lattice is only slightly affected by PVWG addition. The relatively stable APF values suggest that the glass phase primarily resides at grain boundaries rather than substituting into the crystal lattice. The theoretical density (ρ_{th}) calculated from the unit cell parameters exhibits values ranging from 5.947 to 6.315 g cm^{-3}, which are consistent with previously reported densities for BNT ceramics. Although the theoretical density slightly increases at intermediate PVWG contents due to lattice contraction, the overall variation remains moderate, indicating that the fundamental crystal structure is largely preserved. The XRD analysis demonstrates that photovoltaic waste glass acts primarily as a structural modifier rather than a lattice-substituting dopant. The PVWG additive forms an amorphous phase that gradually increases with composition while maintaining the perovskite crystal structure of the BNT matrix. The presence of this glassy phase promotes crystallite growth, reduces dislocation density, and relaxes lattice strain without destabilizing the cubic perovskite framework. These structural modifications play a crucial role in determining the subsequent microstructural evolution and functional properties of the BNT-PVWG ceramics.

The results obtained in this study are consistent with previous reports on glass-modified ferroelectric ceramics, where the introduction of a silicate glass phase has been shown to improve densification and reduce structural defects (Shi et al., 2023; Zhang et al., 2024). The XRD analysis shows that photovoltaic waste glass is mostly a glass-phase engineering agent and not a lattice-substituting dopant. Its addition causes a controlled rise in the amount of amorphous phase, encourages crystallite growth through liquid-phase sintering, and effectively relieves lattice strain without destabilizing the perovskite framework. These changes to the structure are very important for understanding the improved dielectric reliability and energy storage performance that will be discussed in later sections.

Table 3
Crystallite size (D, nm) and lattice strain (ε) determined by Williamson–Hall method.

Sample	Crystallite size, D (W-H) (nm)	Lattice strain, ε ($\times 10^{-3}$)
BNT-00	18.7 ± 0.7	13.2 ± 0.3
BNT-02	21.3 ± 0.8	11.6 ± 0.3
BNT-04	23.8 ± 0.8	10.5 ± 0.2
BNT-06	25.9 ± 0.9	9.6 ± 0.2
BNT-08	27.6 ± 1.0	9.0 ± 0.2
BNT-10	28.8 ± 1.0	8.5 ± 0.2

3.2. Vibrational bonding characteristics revealed by FTIR spectroscopy

Fourier-transform infrared spectroscopy (FTIR) was employed to further examine the local bonding environment and short-range structural features of the BNT-PVWG ceramics. The corresponding spectra are presented in Fig. 4, and Table 5 lists the main vibrational bands and their structural assignments. The FTIR spectra obtained in the range of 400-4000 cm^{-1} show characteristic absorption bands associated with both the perovskite lattice and the silicate glass phase introduced by photovoltaic waste glass (PVWG), thus giving complementary information to the long-range structural analysis from XRD mentioned in Section 3.1.

The strong absorption band in the range of 560-620 cm^{-1} is assigned to the Ti-O stretching vibration of the TiO_6 octahedra, the fundamental structural units of the ABO_3 perovskite lattice. The persistence of this band in all the compositions confirms that the perovskite framework of BNT is retained after PVWG incorporation. This observation is in line with the XRD results that indicate no formation of secondary crystalline phases. This frequency range have been widely reported for BNT and related perovskites such as $BaTiO_3$ and $Pb(Zr,Ti)O_3$ for similar Ti-O vibrational modes. The Ti-O absorption band is significantly broadened and slightly asymmetric with increasing the PVWG content. Importantly, this behavior should not be interpreted as an increase in long-range lattice strain, as XRD analysis shows clear reduction in microstrain (Section 3.1). The FTIR band broadening however indicates the increase of the local structural disorder on the short-range scale, especially in the local environment of TiO_6 octahedra. This difference is due to the different sensitivities of the two techniques, with XRD probing the long-range periodicity and the average lattice distortion and FTIR probing the local bonding heterogeneity. The presence of PVWG results in the formation of an amorphous intergranular phase and heterogeneous interfaces, which can locally distort Ti-O bond angles and lengths with no significant increase in the general lattice strain. The FTIR and XRD results are therefore not contradictory but complementary, describing the structural evolution at different length scales.

Another important feature is the broad absorption band appearing in the region of 1000-1100 cm^{-1}. The band gets stronger and stronger with

Table 4
Effect of PVWG doping ratio in BNT system on parameters of FWHM, dislocation density (δ), atomic packing factor (APF), bond length ($L_{A\text{-}O}$ and $L_{B\text{-}O}$) in perovskite structures, tolerance factor (t), and theoretical density (ρ_{th}).

Sample	FWHM (β, rad)	δ ($\times 10^{-3}$ nm^{-2})	APF	L_{A-O} (Å)	L_{B-O} (Å)	t	ρ_{th} (g/cm^3)
BNT-00	0.00746	2.668	0.740	2.755	1.948	0.982	5.947
BNT-02	0.00652	2.036	0.739	2.758	1.951	0.985	5.926
BNT-04	0.00590	1.671	0.741	2.753	1.947	0.981	5.958
BNT-06	0.00552	1.460	0.748	2.701	1.910	0.968	6.315
BNT-08	0.00518	1.288	0.745	2.722	1.924	0.974	6.170
BNT-10	0.00497	1.185	0.744	2.727	1.928	0.976	6.133

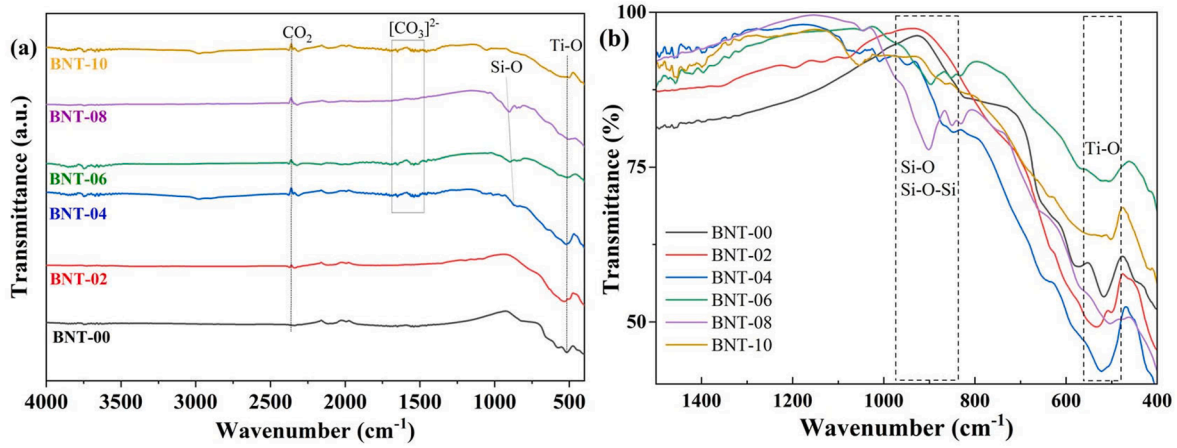

Fig. 4. FTIR spectra of BNT–PVWG ceramics illustrating the evolution of lattice vibrations and silicate glass bonding with increasing PVWG content.

Table 5
Characteristic FTIR vibration bands and their structural assignments in PVWG-doped BNT ceramics.

No.	Wavenumber (cm^{-1})	Vibration	Sources
1	~3400	O–H stretching	hydroxyl/water adsorption
2	~1630	H–O–H bending	water adsorption
3	~1400–1450	CO_3^{2-} vibration	carbonate
4	~1000–1100	Si–O–Si asymmetric stretching	PVWG
5	~800–850	Si–O bending	silicate network
6	~560–620	Ti–O stretching	BNT perovskite networks

increasing PVWG content. This band is assigned to the asymmetric stretching vibration of Si-O-Si bonds in the silicate network. The progressive enhancement of its intensity is direct spectroscopic evidence for the formation and growth of an amorphous glass phase in the ceramic matrix. This trend is in good agreement with the phase analysis of XRD where the amorphous fraction increases from 1.52% in BNT-00 to 12.43% in BNT-10 with increasing PVWG content. The absence of sharp silicate-related peaks further confirms that the glass phase remains mainly amorphous after sintering, rather than crystallizing to form secondary silicate phases.

The additional weak absorption bands at ~3400 cm^{-1} and 1630 cm^{-1} are due to the O-H stretch and H-O-H bend, respectively, because of adsorbed moisture on the surface of the ceramic. A weak band at approximately 1400-1450 cm^{-1} is assigned to carbonate (CO_3^{2-}) vibrations, mostly likely arising from adsorption of atmospheric carbon dioxide during sample handling. These features are typical of oxide ceramics and have little influence on the bulk structural properties.

The FTIR results provides strong evidence for the coexistence of a crystalline perovskite phase and the amorphous silicate network in the PVWG-doped BNT system. The increasing interfacial interaction between the glass phase and the BNT grains is indicated by progressive enhancement of Si-O-Si vibrations together with localized broadening of Ti-O band. These interactions are expected to influence the grain boundary chemistry, the distribution of defects and the local polarization behavior, which are critical factors for the electrical and energy storage performance discussed in the following sections.

3.3. Microstructural evolution and quantitative grain size analysis

Fig. 5 shows the systematic investigation of microstructural evolution of the PVWG-doped BNT ceramics by scanning electron microscopy (SEM). All the micrographs were taken with a JEOL JSM-IT200 microscope at an accelerating voltage of 10 kV and a working distance of ~12 mm. The samples were coated a thin layer of conductive gold was deposited to reduce the surface charging effects during observation. All images are shown with the scale bar (1 μm) to facilitate quantitative interpretation of grain morphology. The undoped BNT-00 sample (Fig. 5 (a)) shows a relatively heterogeneous microstructure with irregular grains morphology and the presence of noticeable intergranular pores. Such features are ascribed to volatilization of Bi and Na species during sintering that results in incomplete densification and defect formation. With the introduction of PVWG (BNT-02 and BNT-04, Fig. 5(b, c)), the microstructure appears to be more compact with better grain packing and less porosity. Such densification improvement is attributed to the liquid-phase-assisted sintering caused by the silicate glass phase that facilitates mass transport along grain boundaries.

Grain size distributions were quantified by ImageJ analysis of more than 250 sizes of grain per sample and histogram fitting using Origin software for statistical reliability. Fig. 6 shows the grain size distributions and Lorentzian fitting results, with the mean grain sizes and standard deviations summarized below: BNT-00: 0.687 ± 0.269 μm; BNT-02: 0.641 ± 0.275 μm; BNT-04: 0.638 ± 0.221 μm; BNT-06: 0.635 ± 0.297 μm; BNT-08: 0.636 ± 0.291 μm; BNT-10: 0.654 ± 0.302 μm. The results indicate that the average grain size for all compositions is within a relatively narrow range (~0.63-0.69 μm)

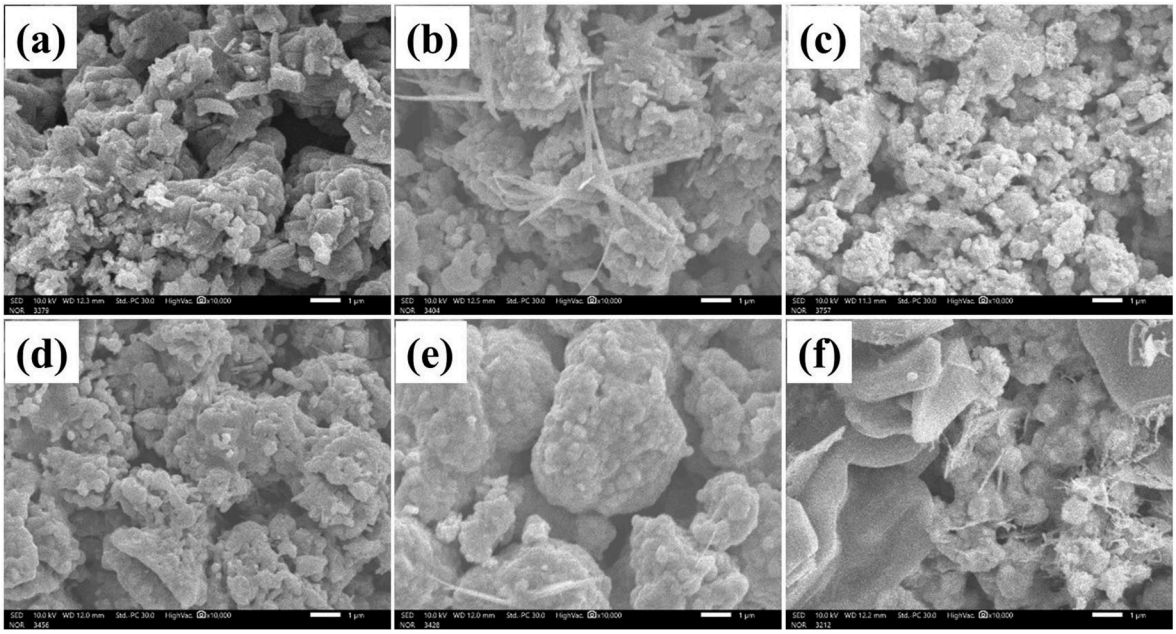

Fig. 5. SEM micrographs showing the microstructural evolution and grain morphology of PVWG-doped BNT ceramics with increasing photovoltaic waste glass content of samples BNT-00 (a), BNT-02 (b), BNT-04 (c), BNT-06 (d), BNT-08 (e), and BNT-10 (f).

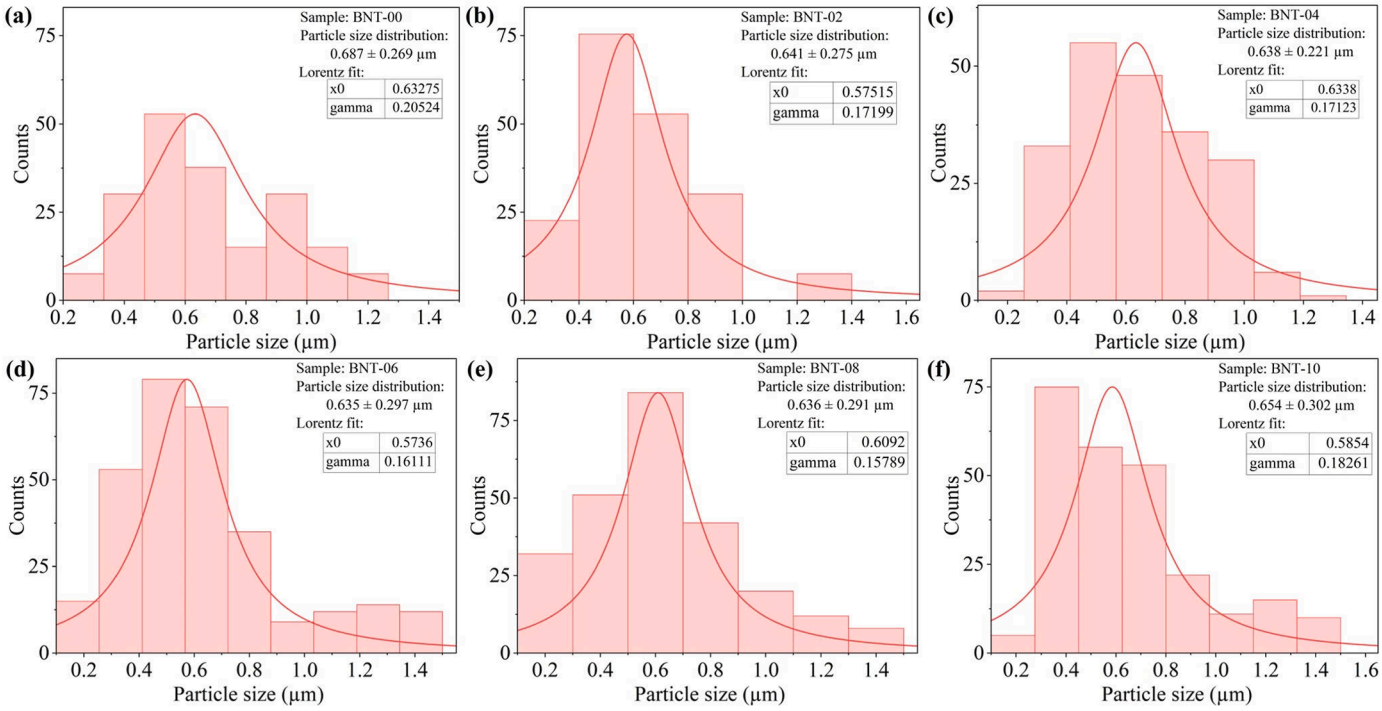

Fig. 6. Histograms for particle size distribution of PVWG-doped BNT ceramics with increasing photovoltaic waste glass content of samples BNT-00 (a), BNT-02 (b), BNT-04 (c), BNT-06 (d), BNT-08 (e), and BNT-10 (f) observed from SEM micrographs via ImageJ and Origin software with Lorentz fit.

with the standard deviation values suggesting a moderately broad size distribution. It should be noted that the introduction of PVWG leads to a slight refinement of the grain size at low doping levels (2-6 wt%) and a marginal increase at higher concentrations (8-10 wt%). This behavior is indicative of a competition between liquid-phase-enhanced densification and inhibition of grain growth because of the accumulation of intergranular glass.

The Lorentzian fitting curves also suggest that the grain size distributions are more symmetric and slightly narrower for intermediate PVWG contents (BNT-04 to BNT-08), showing improved microstructural homogeneity. However, at the highest PVWG content (BNT-10), the distribution broadens again, indicating localized glass-rich regions that partially impede grain coalescence. Observations of SEM images (Fig. 5 (d-f)) show that for intermediate PVWG contents (6-8 wt%) the grains are more equiaxed and evenly dispersed with minimal residual porosity. It suggests that the amorphous glass phase plays the role of a grain boundary modifier that reduces the interfacial energy and stabilizes the microstructure during sintering. At the highest PVWG concentrations

(10 wt%) a small increase in intergranular glass accumulation is observed which may lead to the formation of localized amorphous pockets. It should be noted that the grain size obtained from SEM (micrometer scale) is totally different from the crystallite site obtained from XRD (nanometer scale, 19-29 nm). The crystallite size represents the size of coherent diffraction domains. The size of agglomerated polycrystalline grains (composed of multiple crystallites) is the SEM grain size. So, there is a qualitative rather than quantitative relation between these two parameters. Both parameters show a general trend of structural coarsening with addition of PVWG but they reflect different length scales of structural organization in the present study.

The SEM and statistical grain size analysis indicates that photovoltaic waste glass has two roles in the BNT system: (i) helping in densification by liquid-phase sintering, and (ii) change of the grain boundary structure through the formation of an amorphous intergranular phase. These microstructural features are in accordance role in the electrical conduction behavior and energy storage performance discussed in the following sections.

3.4. Densification and stability of PVWG-doped BNT ceramics

3.4.1. Densification behavior and physical parameters

The densification behavior of the PVWG-doped BNT ceramics was quantitatively evaluated by bulk density, apparent porosity, and relative density as summarized in Fig. 7(a). All values are shown as mean ± standard deviation obtained from at least three independent measurements ($n \geq 3$) to ensure statistical reliability. The bulk density of undoped BNT-00 sample is approximately 5.92 ± 0.03 g cm^{-3}, corresponding to a relative density of 93.4 ± 0.28 % and an apparent porosity of 6.37 ± 0.25 %. These values agree with the heterogeneous microstructure observed in Section 3.3, where the presence of irregular grains morphology and residual porosity was identified. Such incomplete densification is usually ascribed to volatilization of Bi and Na during sintering, leading to pore formation and weak grain boundary cohesion. The addition of PVWG leads to a steady improvement in densification. The relative density goes up to 94.35 ± 0.26% and 95.61 ± 0.24%, while the bulk density goes up to 5.98 ± 0.02 g cm^{-3} (BNT-02) and 6.05 ± 0.2 g cm^{-3} (BNT-04). At the same time, the apparent porosity drops to 5.46 ± 0.22 % and 4.25 ± 0.20 %, respectively. This trend is a direct result of the role of PVWG in promoting liquid-phase-assisted sintering. In this process, the silicate-rich glass softens and form a viscous intergranular phase that makes it easier for particles to move and change shape.

Adding more PVWG, up to 6-8 wt%, makes the densification work best. The BNT-06 and BNT-08 samples have bulk densities of 6.09 ± 0.02 and 6.12 ± 0.03 g cm^{-3}, respectively. Their relative densities are 96.48 ± 0.23% and 97.04 ± 0.21%. The apparent porosity is reduced to 3.64 ± 0.18% (BNT-06) and 3.16 ± 0.15 % (BNT-08). These results are in excellent agreement with the SEM observations presented in Fig. 5, which indicate that the microstructure becomes highly compact and homogeneous, and with XRD results (Section 3.1), which demonstrate reduced lattice strain and defect density. At the highest PVWG content (10 wt%), there is a small drop in densification. The bulk density goes down to 6.08 ± 0.03 g cm^{-3}, the relative density goes down to 96.27 ± 0.25%, and the porosity goes up to 3.88 ± 0.17%. This behavior is related to the rise in the amorphous phase fraction (~12.43%, Section 3.1) and the localized glass accumulation seen in SEM images (Section 3.3). Too much glass phase can make it harder for grains to come together and create amorphous areas that are weaker mechanically, which can make the whole thing a little less compact. The densification behavior shows a clear non-linear relationship with the amount of PVWG, with an optimal glass-phase sintering and structural integrity.

3.4.2. Mechanical stability and hardness enhancement

The mechanical properties of the PVWG-doped BNT ceramics were evaluated using Vickers indentation tests, and the corresponding results are illustrated in Fig. 7(b). The measurements were taken with a microhardness tester that had a load of 1 kgf and dwell time of 15 s. At least five indentations were done for each composition ($n \geq 5$), and the values given are the average with standard deviation. The undoped BNT-00 ceramic sample has a Vickers hardness of 4.22 ± 0.12 GPa and a fracture toughness of 1.15 ± 0.04 MPa m$^{1/2}$. These comparatively low values are ascribed to residual porosity and inadequate grain boundary adhesion, as validated SEM analysis (Section 3.3). As the amount of PVWG goes up, both hardness and fracture toughness go up a lot. The hardness rises to 4.45 ± 0.10 GPa (BNT-02), 4.81 ± 0.11 GPa (BNT-04), and 5.34 ± 0.09 GPa (BNT-06), and the fracture toughness rises to 1.22 ± 0.05, 1.35 ± 0.06, and 1.41 ± 0.05 MPa m$^{1/2}$, respectively. This improvement is mostly due to better densification and stronger grain boundary cohesion caused by the glass phase.

The best mechanical performance is seen in BNT-08, which has a hardness of 5.63 ± 0.08 GPa and a fracture toughness of 1.48 ± 0.06 MPa m$^{1/2}$. This is because it has high relative density (97.04%). The amorphous intergranular phase effectively strengthens grain boundary while keeping the structure intact at this composition. FTIR results (Section 3.2) provide additional support for this

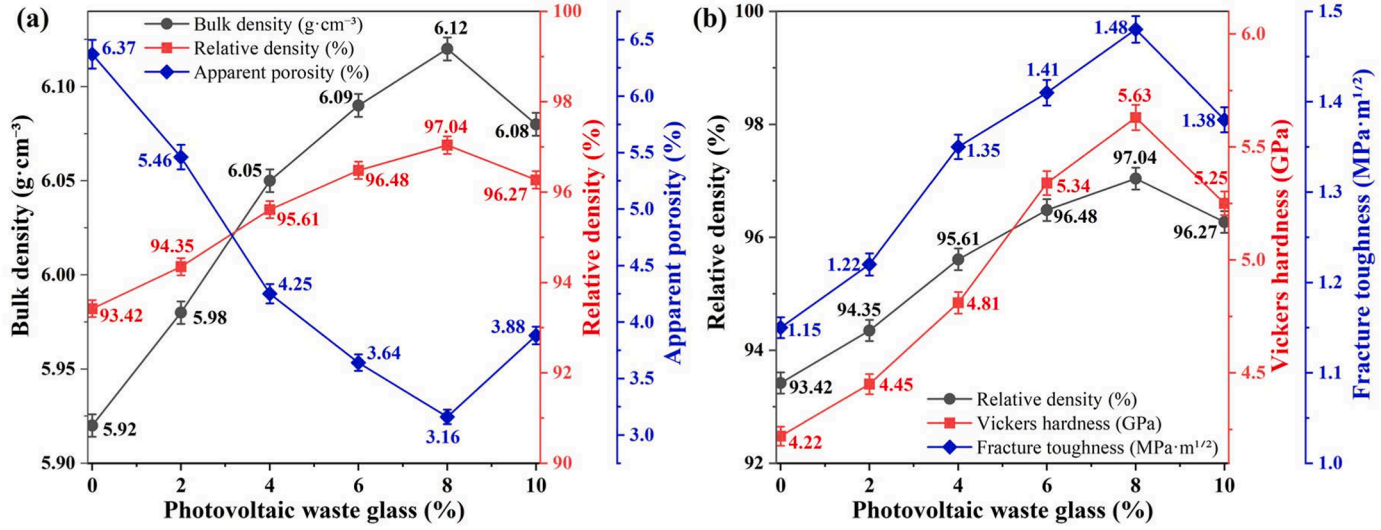

Fig. 7. Variation of bulk density, relative density and apparent porosity (a); correlation and evolution among relative density and Vickers hardness as well as fracture toughness (b) of PVWG-doped BNT ceramics as a function of PVWG content.

interpretation by demonstrating improved Si-O-Si bonding, which enhances interfacial strength. When the PVWG content is higher (BNT-10), the hardness (5.25 ± 0.10 GPa) and fracture toughness (1.38 ± 0.05 MPa $m^{1/2}$) go down a little bit. This decrease is due to too much glass building up, which makes some areas mechanically softer and facilitate crack propagation. This trend is consistent with the XRD results (Section 3.1), where the amorphous fraction went up, and in SEM (Section 3.3), where the grain size distribution got wider. This study used the Anstis equation to figure out the fracture toughness (K_{IC}). This equation connects indentation load, crack length, and hardness. This method is widely used for brittle ceramics and gives a good estimate of how well they can resist cracks. The mechanical properties are closely linked to densification and changes in the microstructure. Adding PVWG makes things harder and more resistant to breaking by: reducing porosity; strengthening grain boundaries; and creating a flexible amorphous intergranular phase. But too much glass can cause local softening effects that make the returns less valuable. These results show how important optimized glass-phase engineering is for making BNT-based ceramics that are strong and dense.

3.5. Defect-mediated charge transport and thermally activated conduction in PVWG-doped BNT ceramics

3.5.1. Temperature-dependent electrical conductivity

The temperature-dependent electrical conductivity (σ) of the PVWG-doped BNT ceramics is shown in Fig. 8(a). All compositions display a monotonic increase in conductivity with temperature (300-600 K), which is the feature of a typical thermally activated semiconducting behavior. Results are expressed as mean ± SD ($n \geq 3$) and error bars indicate the statistic reliability of the measured values. The electrical conductivity of the undoped sample (BNT-00) increases from 0.042 ± 0.001 mS cm^{-1} at 300 K to 7.373 ± 0.131 mS cm^{-1} at 600 K. This relatively low conductivity is consistent with its microstructural features (Section 3.3), with significant porosity and poor grain connectivity lead to high grain boundary resistance. Therefore, the activation energy is relatively high (E_a = 0.849 ± 0.002 eV, Fig. 8(d)), indicating that charge carriers require a significant amount of thermal energy to overcome the barriers related to defects and boundaries.

A significant increase in conductivity is observed upon the introduction of PVWG. The sample BNT-02 shows the highest conductivity of 19.832 ± 0.313 mS cm^{-1} at 600 K with lower activation energy E_a = 0.793 ± 0.002 eV. BNT-04 also has a relatively high conductivity (13.882 ± 0.146 mS cm^{-1}) and the lowest activation energy of 0.783 ± 0.002 eV. This improvement is directly correlated density increased from 93.42 (BNT-00) to 96.48% (BNT-04) and the porosity significantly decreased.

The increased conductivity at low PVWG content (≤4 wt%) is attributed to: improved grain packing and decreased porosity (Section 3.4), increased grain connectivity observed in SEM (Section 3.3), decreased lattice strain and defect density from XRD (Section 3.1). Together these factors reduce possible barriers to charge transport and thus promote thermally activated hopping conduction. However, for higher PVWG contents (>4 wt%), the conductivity decreases even at further densification. For example: BNT-06: 9.612 ± 0.131 mS cm^{-1}, E_a = 0.798 eV; BNT-08: 8.457 ± 0.128 mS cm^{-1}, E_a = 0.812 eV; BNT-10: 7.994 ± 0.124 mS cm^{-1}, E_a = 0.826 eV. This non-monotonic behavior is an indication of a change of the prevailing conduction mechanism. Still, densification is improving, but the amount of amorphous glass phase at

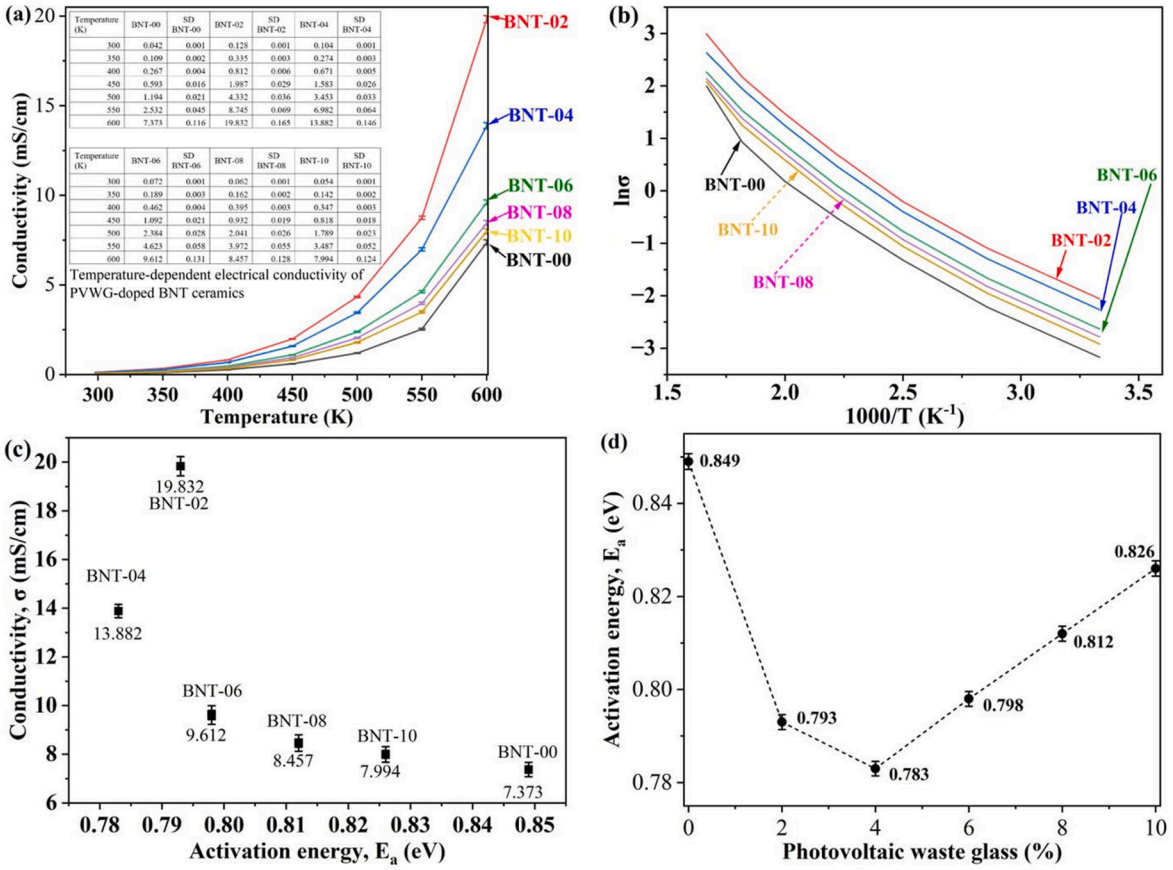

Fig. 8. Temperature-dependent electrical conductivity of PVWG-doped BNT ceramics illustrating the influence of photovoltaic waste glass on charge transport behavior (a); Arrhenius plots (lnσ vs 1000/T) of PVWG-doped BNT ceramics used to determine activation energy for electrical conduction (b); Correlation between activation energy and electrical conductivity in PVWG-doped BNT ceramics (c); and Variation of activation energy with PVWG concentration in BNT ceramics (d).

grain boundaries is too high, which results in the formation of electrically insulating intergranular layers. These layers enhance the grain-boundary resistance and partly inhibit the long-range charge transportation.

Therefore, PVWG has two functions in electrical transport: (i) at low content (≤4 wt%), enhances conductivity via densification and connectivity, and (ii) at higher content (>4 wt%), decreases conductivity due to segregation of the insulating glass phase at grain boundaries. This agrees with the microstructural evolution observed in the SEM where excessive glass leads to localized amorphous regions. Importantly, the observed improvement of insulation and breakdown strength reported in later sections is not in contradiction with the observed increase in conductivity at low PVWG content. Instead, it represents a de-coupling between the DC conductivity and the dielectric breakdown behavior, where: Enhanced carrier mobility leads to a moderate rise in conductivity; Breakdown strength is affected by defect distribution, uniformity of grain boundaries, and local field homogenization.

3.5.2. Arrhenius analysis and conduction mechanism

The temperature dependent conductivity was analyzed by Arrhenius equation (Petrowsky & Frech, 2009) to quantitatively evaluate the conduction mechanism:

$$\sigma = \sigma_0 \exp\left(\frac{E_a}{kT}\right)$$

where σ is the electrical conductivity, σ_0 is the pre-exponential factor, E_a is the activation energy for conduction, k is the Boltzmann constant, and T is the absolute temperature. The resulting Arrhenius plots (lnσ versus $1000/T$) are shown in Fig. 8(b), and the slopes of the linear fits were used to determine the activation energies shown in Fig. 8(c) and (d).

The extracted activation energies are in the range of 0.783 eV (BNT-04) to 849 eV (BNT-00). The range is typical of oxygen-vacancies-mediated conduction ($V_O^{\cdot\cdot}$) in perovskite oxides. The conduction mechanism can be explained by the defect reaction (Thang, 2026; Thang & Hien, 2026):

$$O_O \rightarrow V_O^{\cdot\cdot} + \frac{1}{2}O_2 + 2e^-$$

where oxygen vacancies ($V_O^{\cdot\cdot}$) are mobile charge carriers that mediate hopping conduction. Fig. 8(c) shows a clear inverse correlation between activation energy and conductivity: lower activation energy leads to higher conductivity. The optimized composition, BNT-04, shows the lowest energy barrier (0.783 eV) with high conductivity suggesting efficient charge transport pathways.

The importance of PVWG in the modification of defect chemistry can be understood as follows: at low doping levels, PVWG reduces the resistance of the grain boundaries and encourages hopping of carriers; at high doping levels, amorphous silicate phases form potential barriers, resulting in increased activation energy. The results are strongly supported by the structural and microstructural analysis: XRD analysis shows the lower lattice strain and defect density; FTIR analysis presents the higher local structural disorder; SEM characteristics show the better grain uniformity and then glass segregation; Densification describes the higher density at intermediate PVWG content. In this work, impedance spectroscopy was not used but the single activation energy and the systematic trends found are strong indications for a mixed grain-grain boundary conduction mechanism, where the grain boundary contribution is predominant for higher PVWG concentrations. The results demonstrate that PVWG serves as a microstructural and defect engineering modifier that enables the tunability of electrical transport behavior in BNT ceramics via controlled glass-phase incorporation.

3.6. Energy storage characteristics of PVWG-doped BNT ceramics

3.6.1. Polarization behavior and hysteresis characteristics

The energy storage properties of the PVWG-modified BNT ceramics were systematically studied based on the polarization-electric field (P-E) hysteresis loops at high electric fields. Fig. 9 shows representative P-E hysteresis loops, and the extracted energy storage parameters are summarized in Fig. 10 and Table 6 with mean values and standard deviation from at least three independently prepared specimens ($n \geq 3$). The

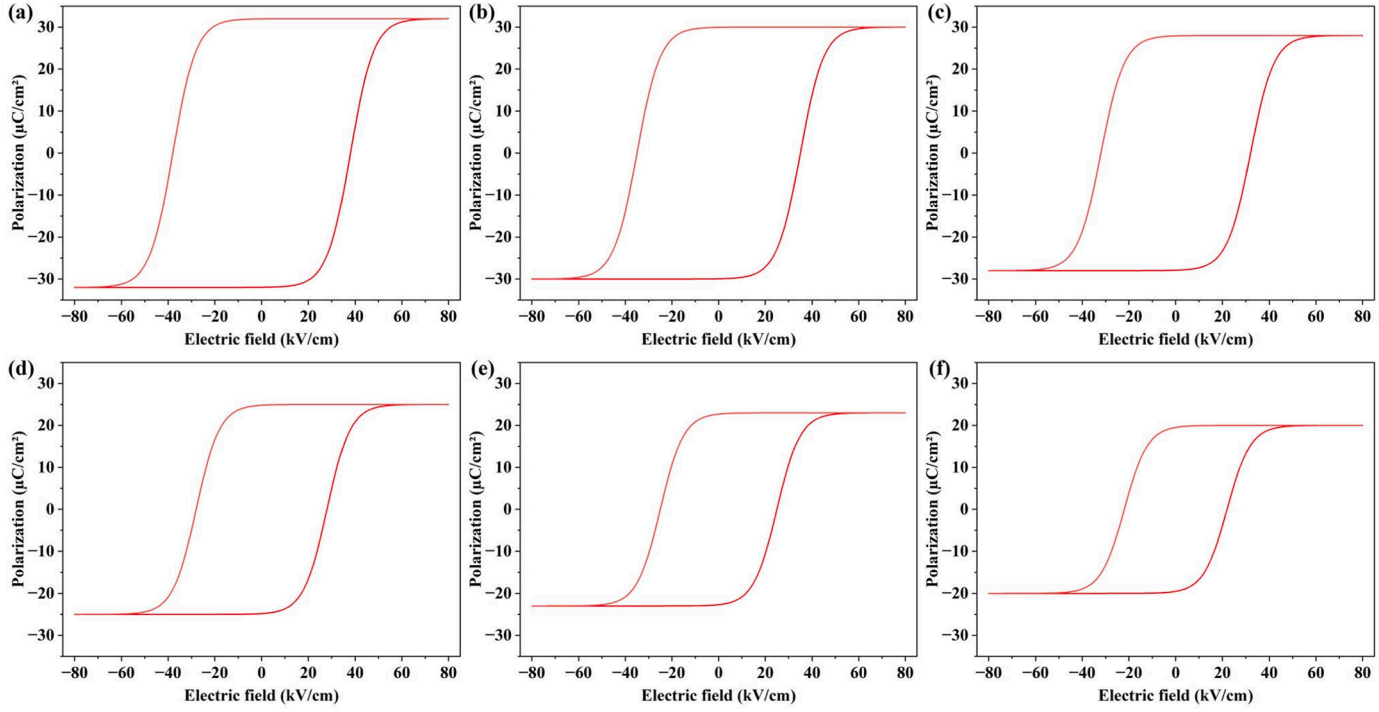

Fig. 9. Polarization-electric field (P-E) hysteresis loops of PVWG-doped BNT ceramics measured at various electric fields for samples of BNT-00 (a), BNT-02 (b), BNT-04 (c), BNT-06 (d), BNT-08 (e), and BNT-10 (f).

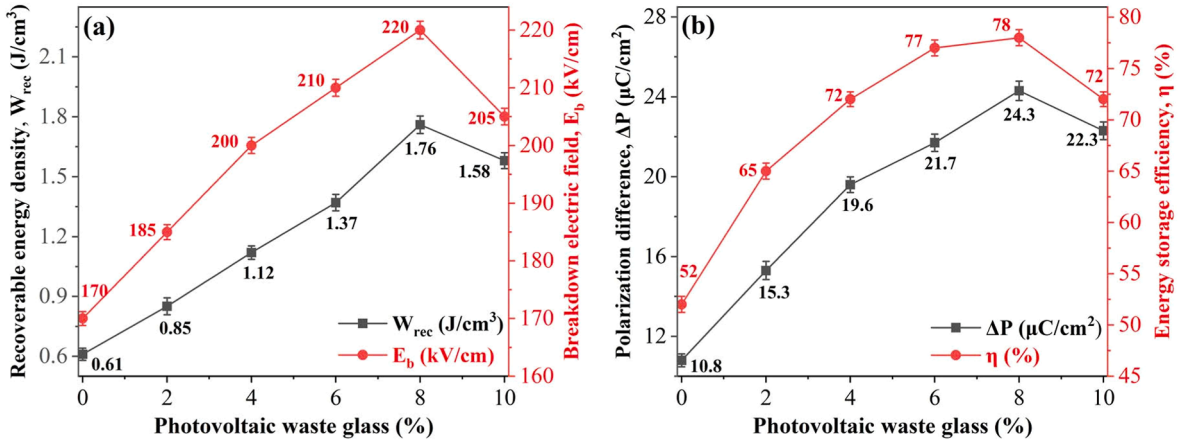

Fig. 10. (a) Evolution of breakdown strength (E_b) and recoverable energy density (W_{rec}) of PVWG-doped BNT ceramics as a function of photovoltaic waste glass content, including standard deviation error bars; (b) Variation of energy storage efficiency (η) and polarization difference (ΔP=P_{max}−P_r) with PVWG concentration in PVWG-modified BNT ceramics.

undoped BNT ceramic (BNT-00) shows a typical ferroelectric hysteresis loop with relatively large remanent polarization and broad loop area, indicating the significant irreversible domain switching. The sample shows a maximum polarization (P_{max}) of 29.4 ± 0.3 μC cm^{-2}, a remanent polarization (P_r) of 18.6 ± 0.5 μC cm^{-2} and a coercive field (E_c) 0f 42 ± 1 kV cm^{-1} in quantitative terms. The relatively large remanent polarization leads to a small recoverable polarization difference (ΔP=P_{max} − P_r) of only 10.8 μC cm^{-2}, thus limiting the recoverable energy density (W_{rec}) to 0.61 ± 0.04 J cm^{-3} with an energy storage efficiency (η) of ~52 ± 2 % under a breakdown electric field (E_b) of 170 ± 5 kV cm^{-1}.

The P-E hysteresis loops progressively thinner and electrically more reversible upon addition of photovoltaic waste glass, suggesting suppression of irreversible ferroelectric domain switching. For the BNT-02 composition, the large decrease of the value of P_r to 15.9 ± 0.4 μC cm^{-2} is accompanied with an increase of the value of P_{max} to 31.2 ± 0.4 μC cm^{-2}, resulting in a much larger polarization difference of 15.3 μC cm^{-2}. Concomitantly, the coercive field increases slightly to 45 ± 1 kV cm^{-1}, indicating modified domain-wall dynamics associated with PVWG-induced grain-boundary regulation. Consequently, the recoverable energy density is remarkably increased to 0.85 ± 0.05 J cm^{-3} with an energy storage efficiency of 65 ± 2 % and a breakdown strength of 185 ± 4 kV cm^{-1}. Aa additional improvement of the reversibility of the polarization is observed for the BNT-04 and BNT-06 compositions. The remanent polarization decreases continuously from 13.2 ± 0.4 μC cm^{-2} to 11.8 ± 0.3 μC cm^{-2}. The maximum polarization increases to 32.8 ± 0.5 μC cm^{-2} and 33.5 ± 0.6 μC cm^{-2}, respectively. Consequently, the polarization difference increases from 19.6 to 21.7 μC cm^{-2}. The narrower hystereisis loops imply more reversible polarization behavior, which is very desirable for the dielectric capacitor applications because a larger portion of the stored electrostatic energy can be released upon the discharge. Thus, the recoverable energy density is improved to 1.12 ± 0.06 J cm^{-3} (BNT-04) and 1.37 ± 0.07 J cm^{-3} (BNT-06), and the energy storage efficiencies enhanced to ~72 and 77 %, respectively.

The evolution of the hysteresis behavior is strongly related to the structural and microstructural changes induced by PVWG addition. The XRD analysis (Scherrer and Williamson-Hall methods) in Section 3.1 indicated that the addition of PVWG decreased the lattice strain and the dislocation density, and increased crystallite size. The structural relaxation diminishes the defect-assisted domain pinning and favors more reversible polarization switching. On the other hand, FTIR results indicated a gradual formation of an amorphous silicate phase via continuous increase of the Si-O-Si vibrational band. The SEM results in Section 3.3 also observed the enhancement of liquid-phase-assisted densification by PVWG, which resulted in a more homogeneous microstructure with lower porosity and better grain connectivity. Quantitative grain-size analysis of more than 250 grains per sample by ImageJ measurements indicated that the average grain size was in the narrow range of 0.635-0.687 μm, and that the grain-size uniformity was improved at intermediate PVWG contents as revealed by the Lorentz fitting profiles. These microstructural refinements directly contribute to the densification behavior described in Section 3.4 where the relative density increased from 93.42 ± 0.15 % for BNT-00 to 97 ± 0.18 % for BNT-08, with a reduction in apparent porosity from 6.37 ± 0.12% to 3.16 ± 0.09%.

Table 6
The energy storage parameters of BNT doping PVWG.

Samples	PVWG (wt %)	P_{max} (μC/cm^2)	P_r (μC/cm^2)	E_c (kV/cm)	W_{total} (J/cm^3)
BNT-00	0	29.4 ± 0.3	18.6 ± 0.5	42 ± 1	1.18 ± 0.04
BNT-02	2	31.2 ± 0.4	15.9 ± 0.4	45 ± 1	1.31 ± 0.05
BNT-04	4	32.8 ± 0.5	13.2 ± 0.4	46 ± 1	1.56 ± 0.06
BNT-06	6	33.5 ± 0.6	11.8 ± 0.3	48 ± 1	1.77 ± 0.07
BNT-08	8	33.7 ± 0.6	9.4 ± 0.3	47 ± 1	2.25 ± 0.07
BNT-10	10	32.5 ± 0.6	10.2 ± 0.3	46 ± 1	2.19 ± 0.07

3.6.2. *Recoverable energy density and efficiency enhancement*

Among all the compositions investigated, the BNT-08 sample exhibited the most optimized energy storage behavior. The P-E loop becomes much thinner at the expense of a relatively high maximum polarization. The sample exhibits P_r = 9.4 ± 0.3 μC cm^{-2} and P_{max} = 33.7 ± 0.6 μC cm^{-2}, corresponding to the highest polarization difference of 24.3 μC cm^{-2}. At the same time, the breakdown electric field (E_b) is 220 ± 6 kV cm^{-1}, which is much higher than that of the undoped BNT sample (170 ± 5 kV cm^{-1}). The BNT-08 composition exhibits the maximum recoverable energy density of 1.76 ± 0.07 J cm^{-3} and energy storage efficiency of 78 ± 2 %. The improved energy storage performance is due to several synergistic effects arising from the optimized PVWG concentration. First, the reduced lattice strain and the improved crystallinity in Section 3.1 allow stable polarization switching under high electric fields. Second, the improved densification and decreased porosity (discussed in Section 3.3 and 3.4) inhibit the local electric-field concentration and avoid dielectric breakdown, leading to increased dielectric breakdown strength. Thirdly, the electrical transport analysis in Section 3.5 revealed that moderate addition of PVWG decreases the activation energy from 0.849 eV (BNT-00) to 0.783 eV (BNT-04), suggesting improved carrier mobility and grain-boundary connectivity. Importantly, the optimized dense microstructure suppresses the excessive leakage pathways by reducing the pore related

defects and intergranular scattering centers although the conductivity increases at low PVWG concentrations. Therefore, the improvement of breakdown strength is not in contradiction with the moderate increase in conductivity, but reflects the balance between the improved grain connectivity and the controlled grain-boundary insulation. This balance results in an efficient polarization switching at intermediate PVWG contents but also provides sufficient dielectric reliability under high electric fields.

When the PVWG content is further increased to 10 wt%, the energy storage performance is slightly deteriorated. The remanent polarization is still relatively low (10.2 ± 0.2 μC cm^{-2}), while the maximum polarization is slightly reduced to 32.5 ± 0.5 μC cm^{-2}, giving a polarization difference of 22.3 μC cm^{-2}. Simultaneously the breakdown electric field decreases from 220 ± 6 kV cm^{-1} to 205 ± 5 kV cm^{-1} which leads to a decrease in recoverable energy density (W_{rec}) to 1.58 ± 0.07 J cm^{-3} and a reduction in efficiency to 72 ± 2 %. Such behavior was supported by XRD and FTIR results, showing a significant increase of amorphous phase fraction at high PVWG concentrations. A large glass accumulation at grain boundaries can locally break the continuity of polarization and form electrically heterogeneous regions that limit the dielectric reliability.

3.6.3. Energy storage performance and structure-property correlation

The energy storage behavior of the PVWG-doped BNT ceramics is closely related to the synergistic interaction of structural stabilization, grain boundary engineering, densification enhancement, and defect-regulated electrical transport as discussed in the previous sections. Among the compositions, the optimized BNT-08 composition shows the best balance of a high polarization difference ($\Delta P = P_{max} - P_r \sim 24.3$ μC cm^{-2}), enhanced dielectric breakdown strength ($E_b = 220 \pm 4$ kV cm^{-1} for BNT-08), reduced remanent polarization ($P_r = 9.4 \pm 0.3$ μC cm^{-2}), and improved microstructural homogeneity, resulting in the highest recoverable energy density ($W_{rec} = 1.76 \pm 0.07$ J cm^{-3}) and energy storage efficiency ($\eta = 78 \pm 2$ %) among all the compositions studied. The improvements are correlated to the structural and microstructural evolution induced by the PVWG additive. The addition of PVWG led to the reduction of lattice strain and dislocation density, and also promoted liquid-phase assisted densification and more uniform packing of grains, as shown in Sections 3.1 and 3.2. The enhanced dielectric reliability and suppression of premature electrical breakdown were attributed to the optimized densification behavior achieved in Section 3.4, where the relative density increased from 93.42 ± 0.31 % for BNT-00 to 97.04 ± 0.28 % for BNT-08. Meanwhile, the conduction analysis in Section 3.5 revealed that moderate PVWG incorporation induced the reduction of activation energy and enhencement of intergranular transport without excess leakage conduction, which enabled stable polarization switching under higher applied electric fields.

For a more complete evaluation of the importance of the present results, the energy storage performance was compared with representative BNT-based ceramics reported in recent literature, as listed in Table 7. In order to avoid misleading comparisons resulting from the substantially different operating electric fields, the reported systems can be reasonably grouped into three electric-field regimes: low-field systems (≤150 kV cm^{-1}), moderate-field systems (150-230 kV cm^{-1}), and ultrahigh-field systems (>450 kV cm^{-1}). In the low field region, pure BNT ceramics usually exhibit very poor energy storage capability, which is caused by the large remanent polarization and the relatively low dielectric breakdown strength. For example, pure BNT ceramics exhibited a recoverable energy density of only about 0.14 J cm^{-3} under an electric field of ~150 kV cm^{-1} (Wang et al., 2025). This behavior has been partially improved with compositional engineering strategies. Modified (1-x)(BNT-BT)-xNT ceramics achieved $W_{rec} \approx 1.20$ J cm^{-3} with an efficiency of 74.8 % under 100 kV cm^{-1} for Xu et al. (Qi et al., 2016), and defect-engineered BNSBT ceramics reached about 1.80 J cm^{-3} under 110 kV cm^{-1} (Li et al., 2022). The results suggest that the recoverable energy density can be significantly enhanced under relatively low electric fields by appropriate defect and domain engineering compared to the undoped BNT ceramics.

Table 7
Comparison of energy storage performance of BNT-based ceramics reported in recent literature.

Material system	Electric field (kV/cm)	W_{rec} (J/cm^3)	Efficiency η (%)	Reference
(1-x)(BNT-BT)-xNT ceramics	100	1.20	74.8	(Qi et al., 2016)
BNSBT defect-engineered ceramics	110	1.80	-	(Li et al., 2022)
Pure BNT ceramic	~150	0.14	-	(Wang et al., 2025)
0.48BNT-0.12BKT-0.4SST ceramics	189	3.52	92.1	(Huang et al., 2025)
BNT-ST-BBN relaxor ceramics	200	3.97	81	(Zheng et al., 2021)
0.7BNT-0.2BZT-0.1NN ceramics	220	3.53	93.5	(Yang et al., 2024)
0.65BNT-0.35STT ceramics	230	3.30	90.4	(Qiao et al., 2023)
BNT-BT-NMH ternary system	~450	7.82	93.1	(Long et al., 2025)
BNT-NN-SSN ceramic	515	7.22	95.3	(Liu et al., 2024)
BNST-0.08BMT ceramic	565	8.58	93.5	(Wang et al., 2021)
BNT-PVWG (this work)	220	1.76	78	Present work

A more relevant comparison with the present work is possible in the moderate electric field regime (150-230 kV cm^{-1}), where some advanced BNT-based relaxor systems have shown improved energy storage performance by microstructural refinement and polarization modulation. The BNT-ST-BBN relaxor ceramics exhibited $W_{rec} \approx 3.97$ J cm^{-3} with $\eta \approx 81$ % at 200 kV cm^{-1} (Zheng et al., 2021). Likewise, 0.48BNT-0.12BKT-0.4SST ceramics have attained $W_{rec} \approx 3.52$ J cm^{-3} and $\eta \approx 92.1$ % at 189 kV cm^{-1} (Huang et al., 2025). 0.7BNT-0.2BZT-0.1NN relaxor ceramics exhibited $W_{rec} \approx 3.53$ J cm^{-3} with $\eta \approx 93.5$ % at 220 kV cm^{-1} (Yang et al., 2024). Also, Qiao et al. (Qiao et al., 2023) reported $W_{rec} \approx 3.30$ J cm^{-3} and $\eta \approx 90.4$ % for 0.65BNT-0.35STT ceramics under 230 kV cm^{-1}. Relative to these highly optimized relaxor systems, the present BNT-PVWG ceramics exhibit a relatively modest recoverable energy density of 1.76 J cm^{-3} at 220 kV cm^{-1}. Nonetheless, the present system relies on a significantly simplified compositional modification strategy combined with conventional solid-state processing and sustainable incorporation of recycled photovoltaic waste glass. Furthermore, the improvement observed in the present work is mainly attributed to the microstructural densification, reduction of remanent polarization and improvement of breakdown strength induced by PVWG, instead of complex multicomponent relaxor engineering.

By contrast, much higher recoverable energy densities have been reported in multicomponent BNT-based ceramics operating under ultrahigh electric fields above 450 kV cm^{-1}. For example, Wang et al. (2021) reported an ultrahigh energy density of 8.58 J cm^{-3} with an efficiency of 93.5 % in BNST-0.08BMT ceramics under 565 kV cm^{-1} through simultaneous domain and bandgap engineering. Liu et al. (2024) obtained $W_{rec} \approx 7.22$ J cm^{-3} and $\eta \approx 95$ % for BNT-NN-SSN ceramics at 515 kV cm^{-1}, while Long et al. (2025) reported in multicomponent BNT-BT-NMH ternary ceramics with a recoverable energy density of 7.82 J cm^{-3} and an efficiency of 93.1 % at 450 kV cm^{-1}. While these ultrahigh-field systems have substantially higher absolute energy densities, direct comparisons to the present PVWG-modified BNT ceramics must be made with caution because the energy density highly field-dependent and scales approximately as E^2. The moderate but competitive performance attained in the present PVWG-doped BNT ceramics with only 220 kV cm^{-1} thus signifies that recycled

photovoltaic waste glass can be effectively utilized to tailor the structure-microstructure-property relationship of BNT ceramics without the need for excessively high operating electric fields or highly complex compositional engineering.

In general, the present results show that the photovoltaic waste glass acts as a sustainable glass-forming additive for promoting liquid-phase sintering and microstructural densification, but also as an effective functional modifier for regulating the polarization reversibility, dielectric breakdown strength and defect-assisted conduction behavior. Thus, the use of recycled PVWG offers a cost-effective and environmentally friendly way to enhance the energy storage performance of lead-free BNT ceramics for capacitor-type dielectric applications.

4. Conclusion

The environmentally sustainable photovoltaic waste glass (PVWG)-doped $Bi_{0.5}Na_{0.5}TiO_3$ (BNT) ceramics were successfully fabricated by the conventional solid-state reaction route and sintering at 1120 °C for 2 h in this study. The effect of recycled PVWG on structural evolution, microstructural features, densification behavior, electrical transport, mechanical stability and energy storage performance of BNT ceramics was systematically investigated. The results show that PVWG is an effective glass-phase sintering additive to simultaneously tailor grain-boundary properties and enhance the multifunctional properties of lead-free ceramics. The XRD analysis confirmed that all compositions maintained the single-phase perovskite structure of BNT with no evidence of any secondary crystalline phases, suggesting that the incorporation of PVWG did not destabilize the host lattice. However, subtle peak broadening and intensity variation revealed local structural distortion and partial amorphous-phase formation induced by the glass additive. FTIR analysis also confirmed the co-existence of Ti-O/Ti-O-Ti vibrational modes related to the BO6 octahedral framework along with Si-O related bands arising from the silicate glass network. These observations suggest that PVWG induces a structurally altered grain-boundary environment, affecting the distribution of defects and the local polarization behavior. The densification and microstructure homogeneity were substantially improved by the addition of PVWG through a mechanism of glass-assisted liquid-phase sintering. The relative density increased from 93.42 ± 0.18 % for the undoped BNT to 97.04 ± 0.15 % for the optimized BNT-08 composition and the apparent porosity was simultaneously decreased from 6.37 ± 0.21 % to 3.16 ± 0.14 %. SEM observations showed a more homogenous and compact microstructure with improved grain packing and reduced residual pores at intermediate amounts of PVWG. These microstructural features directly contribute to the enhanced mechanical stability, with the Vickers hardness increased from 4.22 ± 0.06 GPa to 5.63 ± 0.08 GPa, and the fracture toughness increased from 1.15 ± 0.03 to 1.48 ± 0.04 MPa $m^{1/2}$ for the BNT-08 ceramic.

Electrical conductivity measurements confirmed the prevalence of thermally activated Arrhenius-type conduction driven by oxygen-vacancy-mediated hopping transport. The activation energy was decreased from 0.849 ± 0.004 eV for BNT-00 to a minimum value of 0.783 ± 0.003 eV for BNT-04, which suggests a reduced grain-boundary resistance and an improved carrier mobility at moderate PVWG contents. However, large amounts of PVWG addition resulted in larger amorphous grain-boundary regions, which slightly increased activation energy and suppressed long-range charge transport. This dual role of PVWG accounts for the non-monotonic evolution of conductivity and indicates that the optimized glass content can be used to balance the enhancement of densification and electrical insulation. More significantly, the energy storage performance of BNT ceramics was significantly enhanced by adding PVWG. The optimized BNT-08 composition exhibits a narrow P-E hysteresis loop with a large polarization difference (ΔP = 24.3 μC cm^{-2}), decreased remanent polarization (P_r = 9.4 ± 0.3 μC cm^{-2}) and improved dielectric breakdown strength (E_b = 220 ± 5 kV cm^{-1}). As a result, a recoverable energy density of 1.76 ± 0.07 J cm^{-3} was obtained with an energy storage efficiency of 78 ± 2 %. This shows an increase of about 2.9-fold in W_{rec} and 1.5-fold in efficiency compared to the undoped BNT ceramic (0.61 ± 0.04 J cm^{-3} and 52 ± 2 %, respectively). The improved performance is attributed to the synergistic effects of the enhanced densification, suppressed porosity, optimized grain-boundary insulation, reduced conduction loss and more reversible polarization switching induced by the PVWG phase.

A comparative analysis with previously reported BNT-based systems also suggests that although the current BNT-PVWG ceramics do not achieve the ultrahigh energy densities of complex multicomponent relaxor systems operating at above 450 kV cm^{-1}, they exhibit a competitive energy storage performance under moderate electric fields (≤220 kV cm^{-1}) based on a significantly simpler and more sustainable compositional strategy. Therefore, recycled photovoltaic waste glass offers a promising low-cost and environmentally responsible approach for improving the dielectric and ferroelectric performances of lead-free ceramics, while contributing to the photovoltaic waste valorization and circular-economy-driven materials engineering. Future work should involve detailed impedance spectroscopy analysis to separate the grain and grain-boundary contributions, Weibull statistical assessment of the dielectric breakdown strength, optimization of the glass-phase distribution, and investigation of hybrid relaxor-engineering approaches to further enhance the recoverable energy density and the long-term reliability under cyclic electrical loading.

CRediT authorship contribution statement

Truong Bach Chien: Project administration, Methodology, Investigation, Funding acquisition, Formal analysis, Data curation, Conceptualization. **Le Phong Phu:** Formal analysis, Data curation. **Nguyen Chi Bao:** Data curation. **Nguyen Ngoc Thien:** Data curation. **Tran Thi Phuong Nghi:** Data curation. **Thach Nguyen Phuc Khuong:** Data curation. **Nguyen Hoc Thang:** Writing – review & editing, Writing – original draft, Visualization, Validation, Supervision, Software, Resources, Project administration, Methodology, Investigation, Funding acquisition, Formal analysis, Data curation, Conceptualization.

Funding

Supported by Ho Chi Minh City University of Industry and Trade, contract no. 220/HĐ-DCT dated July 01, 2025.

Declaration of competing interest

The authors declare that they have no known competing financial interests, personal relationships, or affiliations that could have influenced the work reported in this paper.

No external funding or organization had any role in the design of the study, data collection, analysis, interpretation, or writing of the manuscript.

Acknowledgment

This work was financially supported by Ho Chi Minh City University of Industry and Trade under Contract no. 220/HĐ-DCT dated July 01, 2025.

References

Ahmed Althumairi, N., Hjiri, M., Aldukhayel, A. M., Jbeli, A., & Nassar, K. I. (2025). Recent advances in dielectric and ferroelectric behavior of ceramic nanocomposites: Structure property relationships and processing strategies. *Nanomaterials, 15*(17), 1329. https://doi.org/10.3390/nano15171329

Ahmed, O., Ihyadn, A., Hadouch, Y., Hoummada, K., Mezzane, D., Bih, H., El, M. H., Naji, M., Manoun, B., & Bih, L. (2024). Exploring structural compatibility and energy storage performances enhancement in lead-free BNT dielectric ceramics with NBTP glass integration. *Ceramics International, 50*(13), 24648–24661. https://doi.org/10.1016/j.ceramint.2024.04.199. Part B, 2024.

Azizi, Y., Yazdanmehr, M., Ahmadvand, H., Vahdani, M. R. K., & Ahmadvand, H. (2025). Dielectric, piezoelectric, and ferroelectric properties of Sm3+/Nd3+/Mn2+-doped and Sm3+/Mn2+-, and Nd3+/Mn2+-codoped 0.24PIN-0.46PMN-0.30PT ternary ceramics. *Journal of Electroceramics*. https://doi.org/10.1007/s10832-025-00437-6, 2025.

Cao Hien, N., Thang, N. H., Mahmood, T., Pawlicka, A., Anwar, M., Munir, M., Ghafoor, A., & Khoa, T. Le A. (2025). Simulation, synthesis, and characterization of Ni–Co and its co-doping in ZnO for energy applications. *RSC Advances, 15*(28), 22730–22744. https://doi.org/10.1039/D5RA02746B

Chakrabarti, A., Menon, S., Tarafder, A., & Rahaman Molla, A. (2022). Glass–ceramics: A potential material for energy storage and photonic applications. In K. Annapurna, & A. R. Molla (Eds.), *Advanced structured materials: 178. Glasses and glass-ceramics*. Singapore: Springer. https://doi.org/10.1007/978-981-19-5821-2_10.

Chen, Y., Sun, K., Wang, Z., Tian, J., Xu, D., & Fan, R. (2026). Multielement (Fe, La, Ca, Zr) doping achieves superior dielectric properties and broad-temperature stability in BaTiO3-based ceramics. *Ceramics International, 52*(10), 14783–14791. https://doi.org/10.1016/j.ceramint.2026.02.114

Ecebaş, N., Tran, T. H. T., Fisher, J. G., Lee, J.-S., Choi, W.-J., Han, Y.-B., & Jo, W. (2026). The effect of sintering atmosphere and temperature on densification, grain growth behavior and electrical properties of 0.685(Na0.5Bi0.5)TiO3-0.065BaTiO3-0.25SrTiO3 ceramics. *Crystals, 16*(2), 143. https://doi.org/10.3390/cryst16020143

Gao, P., Geng, W., Liu, C., Wang, H., Ling, Y., Li, Y., Wan, H., Li, H., & Ren, X. (2025). Design of BNT-based ceramics with enhanced energy density and ultrahigh polarization under moderate electric field via introducing BMW. *Chemical Engineering Journal, 523*(2025), Article 168818. https://doi.org/10.1016/j.cej.2025.168818

Gilmore, C. J., Kaduk, J. A., & Schenk, H. (2019). *International Tables for Crystallography, volume H: Powder diffraction*. First online edition, ISBN 978-1-118-41628-0. https://doi.org/10.1107/97809553602060000115

Guan, X., Lei, Z., Xue, R., Li, Z., Li, P., David, M., Yi, J., Jia, B., Huang, H., Li, X., & Ma, T. (2024). Polarization: A universal driving force for energy, environment, and electronics. *Advanced Materials, 37*, Article 2413525. https://doi.org/10.1002/adma.202413525, 2024.

Huang, Z., He, X., Wang, C. L., Li, J., Huang, L., Zhao, Y., Xu, Y., Gao, S., Peng, L., Liu, Y., Huang, A., & Li, T. (2025). Energy storage performance enhanced and high stability achieved in BNT-Based lead-free ceramics under low electric field via domain engineering. *ACS Applied Materials and Interfaces, 17*(23), 34255–34265. https://doi.org/10.1021/acsami.5c06072, 2025.

Kaarthik, J., Raj, N. P. M. J., Prasad Pabba, D., Peddigari, M., Reddy, S. G., Jang, J., & Venkateswarlu, A. (2026). A review on unlocking the potential of lead-free materials-based energy harvesting systems for standalone electronics. *Smart Materials and Structures, 35*(1), Article 013002. https://doi.org/10.1088/1361-665X/ae2fa3

Khan, S. U., Manan, A., Ullah, A., Qazi, I., Rehman, M. U., Ali Khan, M., Ahmad, A. S., Muhammad, R., & Iqbal, Y. (2025). Dielectric, impedance, and energy storage properties of Bi(Mg0.5Sn0.5)O3 modified Bi0.5Na0.5TiO3 based ceramics. *International Journal of Applied Ceramic Technology, 22*, Article e15030. https://doi.org/10.1111/ijac.15030, 2025.

Khoi, N. H. T., & Thang, N. H. (2026). Low-field strain-driven phase diagram of (Bi1/2Na1/2)TiO3–SrTiO3–LiNbO3 lead-free relaxor ceramics for actuator applications. *RSC Advances, 16*(28), 26173–26189. https://doi.org/10.1039/D6RA00669H, 2026.

Li, Z., Li, D.-X., Shen, Z.-Y., Zeng, X., Song, F., Luo, W., Wang, X., Wang, Z., & Li, Y. (2022). Remarkably enhanced dielectric stability and energy storage properties in BNT-BST relaxor ceramics by A-site defect engineering for pulsed power applications. *Journal of Advanced Ceramics, 11*, 283–294. https://doi.org/10.1007/s40145-021-0532-8, 2022.

Li, D., Shen, Z.-Y., Li, Z., Luo, W., Wang, X., Wang, Z., Song, F., & Li, Y. (2020). P-E hysteresis loop going slim in Ba0.3Sr0.7TiO3-modified Bi0.5Na0.5TiO3 ceramics for energy storage applications. *Journal of Advanced Ceramics, 9*, 183–192. https://doi.org/10.1007/s40145-020-0358-9, 2020.

Li, X., Zhu, C., Li, S., Li, A., Liang, L., Cai, Z., & Feng, P. (2024). Enhancing energy storage density of BNT-ST-based ceramics by a stepwise optimization strategy on the breakdown strength. *Journal of the European Ceramic Society, 44*(11), 6422–6429. https://doi.org/10.1016/j.jeurceramsoc.2024.04.023, 2024.

Liu, J., Li, D., Zhao, W., Xu, D., Shi, Z., Liu, W., Su, J., Zhou, T., Chen, G., & Zhou, Di (2024). Excellent energy storage performance achieved in Sr(Sc0.5Nb0.5)O3-Doped Bi0.5Na0.5TiO3-Based lead-free relaxor ferroelectric ceramics. *ACS Applied Energy Materials, 7*(5), 2030–2038. https://doi.org/10.1021/acsaem.3c03229, 2024.

Long, C., Su, Z., Xu, A., Li, F., Li, Y., Ren, W., Wu, H., Ding, X., & Liu, L. (2025). High energy storage performance in the Bi0.5Na0.5TiO3BaTiO3–Nd(Mg1/2Hf1/2)O3 ternary system with multiscale polymorphic domains and local heterogeneous structure. *Journal of Advanced Ceramics, 14*(4), Article 9221063. https://doi.org/10.26599/JAC.2025.9221063, 2025.

Nguyen, H. T., Binh, N. Q., Van Phuc, N., & Kien, P. T. (2024). Syntheses and characteristics of calcium-based geopolymer from solar-cell panel-glass waste by hydrothermal method. *Materiali in Tehnologije/Materials Technology, 58*(4), 467–475. https://doi.org/10.17222/mit.2024.1153

Njema, G. G., Lemomo, S. N., Tanui, P. K., & Kibet, J. K. (2026). A review of the strategies used in the recovery and passivation of lead in lead-based perovskite solar cells: Balancing device efficiency, toxicity, and environmental sustainability. *Natural Science, 6*(1), Article e70041. https://doi.org/10.1002/ntls.70041, 2026.

Petrowsky, M., & Frech, R. (2009). Temperature dependence of ion transport: The compensated arrhenius equation. *Journal of Physical Chemistry B, 113*(17), 5996–6000. https://doi.org/10.1021/jp810095g, 2009.

Qi, X., Liu, H., Zhang, L., Xie, J., Hua, H., Cao, M., Yao, Z., & Lanagan, M. T. (2016). Structure and electrical properties of lead-free Bi0.5Na0.5TiO3-based ceramics for energy-storage applications check for updates. *RSC Advances, 6*, 59280–59291. https://doi.org/10.1039/C6RA11744A, 2016.

Qiao, X., Liao, A., Chen, B., Zhang, H., Zhang, L., Kong, T., Chao, X., & Yang, Z. (2023). Enhanced energy storage properties of BNT-based ceramics via composition and multiscale structural engineering. *Solid State Sciences, 136*, Article 107090. https://doi.org/10.1016/j.solidstatesciences.2022.107090, 2023.

Ravinshu, R. P., & Thakur, O. P. (2025). Improved transmission and energy storage performance of KNN ceramics with BNT and BKT additives. *Physica Scripta, 100*(7), Article 075978. https://doi.org/10.1088/1402-4896/ade749

Rehman, M. U., Xie, A., Rahman, A., Zhang, Y., Tian, A., Jiang, X., Xie, X., Zhou, C., Li, T., Liu, L., Gao, X., Era, X., & Zuo, R. (2025). Enhanced energy storage performance with excellent thermal stability of BNT-based ceramics via the multiphase engineering strategy for pulsed power capacitor. *Journal of Materials Chemistry C, 13*, 1395–1407. https://doi.org/10.1039/D4TC04170D, 2025.

Shi, X., Li, K., Shen, Z.-Y., Liu, J., Chen, C., Zeng, X., Zhang, B., Song, F., Luo, W., Wang, Z., & Li, Y. (2023). BS0.5BNT-based relaxor ferroelectric ceramic/glass–ceramic composites for energy storage. *Journal of Advanced Ceramics, 12*(4), 695–710. https://doi.org/10.26599/JAC.2023.9220713, 2023.

Soheli, S. N., Lu, Z., Sun, D., & Shyha, I. (2024). Lead-Free NaNbO3-Based ceramics for electrostatic energy storage capacitors. *Ceramics, 7*(2), 712–734. https://doi.org/10.3390/ceramics7020047

Supriya, S. A. (2022). Review on Lead-Free-Bi0.5Na0.5TiO3 based ceramics and films: Dielectric, piezoelectric, ferroelectric and energy storage performance. *Journal of Inorganic and Organometallic Polymers, 32*, 3659–3676. https://doi.org/10.1007/s10904-022-02418-6, 2022.

Tang, L., Pan, Z., Zhao, J., Shen, Y., Chen, X., Li, H., Peng, L., Zhang, Y., Liu, J., & Zhai, J. (2023). Significantly enhanced energy storage capability of BNT-based ceramics via optimized sintering aids. *Journal of Alloys and Compounds, 935*, Article 168124. https://doi.org/10.1016/j.jallcom.2022.168124. Part 2, 2023.

Thang, N. H. (2026). Synthesis strategies of magnetic inorganic nanomaterials to biomedical and spintronic applications. *Chemical Papers*. https://doi.org/10.1007/s11696-026-04706-8, 2026.

Thang, N. H., & Hien, N. C. (2026). Environmental and energy applications of green-synthesized semiconductor nanomaterials: From photocatalysis to smart sensors. *Ionics, 32*, 2521–2556. https://doi.org/10.1007/s11581-025-06940-8, 2026.

Ünsal, Ö. F., Borazan, İ., & Bedeloğlu, A.Ç. (2026). Piezoelectric materials for energy applications. In R. K. Gupta (Ed.), *Handbook of energy materials*. Singapore: Springer. https://doi.org/10.1007/978-981-95-2947-6_49.

Wang, M., Feng, Q., Luo, C., lan, Y., Yuan, C., Luo, N., Zhou, C., Fujita, T., Xu, J., Chen, G., & Wei, Y. (2021). Ultrahigh energy storage density and efficiency in Bi0.5Na0.5TiO3-Based ceramics via the domain and bandgap engineering. *ACS Applied Materials and Interfaces, 13*(43), 51218–51229. https://doi.org/10.1021/acsami.1c14151, 2021.

Wang, Q., Zhang, L., Li, R., Yang, H., Wang, C., Xiong, Z., & Liu, C. (2025). Insight into the structure evolution and performance optimization of Bi0.5Na0.5TiO3-Based ceramics for energy storage application. *Materials, 18*(8), 1801. https://doi.org/10.3390/ma18081801

Weinmann, S., Quincke, L., Winkler, L., Hinricher, J. J., Kurnia, F., Kim, K. J., & Rupp, J. L. M. (2025). Sustainable functional ceramics. *Nature Nanotechnology, 20*, 1729–1745. https://doi.org/10.1038/s41565-025-02076-y, 2025.

Wu, L., He, B., Shuai, Y., Feng, W., Gong, W., Qi, H., & Liu, Y. (2025). Achieving high capacitive energy storage, high-temperature stability and fatigue endurance synchronously at moderate fields in BNT-based ceramics. *Journal of Energy Storage, 132*, Article 117758. https://doi.org/10.1016/j.est.2025.117758. Part B, 2025.

Xie, B., Wu, Q., Yu, C., Wu, S., Zhang, J., Liu, Z., Guo, K., Liu, H., & Li, T. (2026). Local structure strategies promoting lead-free dielectric energy-storage applications. *Small, 22*(11), Article e12097. https://doi.org/10.1002/smll.202512097, 2026.

Yan, F., Huang, K., Jiang, T., Zhou, X., Shi, Y., Ge, G., Shen, B., & Zhai, J. (2020). Significantly enhanced energy storage density and efficiency of BNT-based perovskite ceramics via A-site defect engineering. *Energy Storage Materials, 30*(2020), 392–400. https://doi.org/10.1016/j.ensm.2020.05.026

Yang, H., Cai, Z., Zhu, C., Feng, P., & Wang, X. (2022). Ultra-High energy storage performance in BNT-based ferroelectric ceramics with simultaneously enhanced polarization and breakdown strength. *ACS Sustainable Chemistry; Engineering, 10*(28), 9176–9183. https://doi.org/10.1021/acssuschemeng.2c02155, 2022.

Yang, J., Zhu, X., Wang, H., Zhang, Y., Guan, P., Yan, S., & Zheng, M. (2024). Achieving outstanding energy storage behaviors via combinatorial optimization design in BNT-based relaxor ferroelectric ceramics under medium–low electric fields. *Journal of Materials Chemistry C, 12*, 6479–6486. https://doi.org/10.1039/D4TC00818A, 2024.

Zhang, L., Chen, F., Huang, Y., Jing, R., & Jin, L. (2025). Perspective on polarization regulation for advanced energy storage, 2025 *Applied Physics Letters, 127*(13), Article 130502. https://doi.org/10.1063/5.0288079.

Zhang, X., Han, T., Su, Y., Huang, S., & Huan, Y. (2025). Enhanced temperature stability and electrical performances of PZT-based piezoelectric ceramics for high-temperature ultrasonic transducer application. *Journal of Materials Science, 61*, 10034–10049. https://doi.org/10.1007/s10853-026-12437-0, 2026.

Zhang, L., Jing, R., Zhang, S., & Jin, L. (2026). Multiscale microstructure design for high-performance dielectric energy storage materials. *Microstructures, 6*, Article 2026003. https://doi.org/10.20517/microstructures.2025.89, 2026.

Zhang, H., Tan, H., & Ye, Z.-G. (2024). *Dielectric materials for capacitive energy storage, chapter-inorganic dielectric materials for capacitive energy storage* (1st ed.). Boca Raton: CRC Press. https://doi.org/10.1201/9781003454496. First Published.

Zhang, Z., Wei, H., Li, Q., Yang, N., Dong, P., Zhang, R., Liao, Z., Lin, Z., Fan, H., & Wang, W. (2025). High-entropy and phase engineering induced dislocation networks for improving energy storage in BNT-based ceramics. *Ceramics International, 51*(24), 42211–42219. https://doi.org/10.1016/j.ceramint.2025.06.436. Part B, 2025.

Zheng, B., Fan, J., Chen, B., Qin, X., Wang, J., Wang, F., Deng, R., & Liu, X. (2022). Rare-Earth doping in nanostructured inorganic materials. *Chemistry Review, 122*(6), 5519–5603. https://doi.org/10.1021/acs.chemrev.1c00644, 2022.

Zheng, L., Sun, P., Peng, Z., Bai, W., Li, L., Wen, F., Zhang, J., Wang, N., & Zhang, Y. (2021). Significantly tailored energy-storage performances in Bi0.5Na0.5TiO3–SrTiO3-based relaxor ferroelectric ceramics by introducing bismuth layer-structured relaxor BaBi2Nb2O9 for capacitor application. *Journal of Materials Chemistry C, 9*, 5234–5243. https://doi.org/10.1039/D1TC00437A, 2021.

Zhong, M., Liu, X., Zhu, B., Meng, L., Yuan, C., & Yang, R. (2026). Photocurrent densities and bandgap engineering in A/B-site Co-substituted Bi0.5Na0.5TiO3 ferroelectric semiconductors. *Journal of Alloys and Compounds, 1054, 186311Journal of Alloys and Compounds, 1054*, Article 186311. https://doi.org/10.1016/j.jallcom.2026.186311

Zhou, Q., Peng, Z., Zhang, F., Chai, Q., Wu, Di, Liang, P., Wei, L., Chao, X., & Yang, Z. (2023). Achieving high comprehensive energy storage properties of BNT-based ceramics via multiscale regulation. *Ceramics International, 49*(12), 19701–19707. https://doi.org/10.1016/j.ceramint.2023.03.087, 2023.

Zubairi, H., Lu, Z., Zhu, Y., Reaney, I. M., & Wang, G. (2024). Current development, optimisation strategies and future perspectives for lead-free dielectric ceramics in high field and high energy density capacitors. *Chemical Society Reviews, 53*, 10761–10790. https://doi.org/10.1039/D4CS00536H, 2024.